

Characteristics of Precipitation and Mesoscale Convective Systems over the Peruvian Central Andes in Multi 5-Year Convection-Permitting Simulations

Yongjie Huang¹, Ming Xue^{1,2}, Xiao-Ming Hu^{1,2}, Elinor Martin^{2,3}, Hector
Mayol Novoa⁴, Renee A. McPherson^{3,5}, Changhai Liu⁶, Kyoko Ikeda⁶, Roy
Rasmussen⁶, Andreas F. Prein⁶, Andres Perez⁴, Isaac Yanqui Morales⁴, José
Luis Ticona Jara⁷, and Auria Julieta Flores Luna⁴

¹Center for Analysis and Prediction of Storms, University of Oklahoma, Norman, OK, USA

²School of Meteorology, University of Oklahoma, Norman, OK, USA

³South Central Climate Adaptation Science Center, University of Oklahoma, Norman, OK, USA

⁴Universidad Nacional de San Agustín de Arequipa, Arequipa, Perú

⁵Department of Geography and Environmental Sustainability, University of Oklahoma, Norman, OK, USA

⁶National Center for Atmospheric Research, Boulder, Colorado, USA

⁷Servicio Nacional de Meteorología e Hidrología del Perú (SENAMHI), Arequipa, Perú

Key Points:

- Characteristics of precipitation and MCSs in the Peruvian Central Andes are investigated based on convection-permitting simulations.
- WRF3km_MYNN outperforms in simulating mountain precipitation; both it and WRF4km_SAAG show superior performance in western Amazon.
- Dynamic factors dominate precipitation and MCSs on the Andean east slope, while thermodynamic factors are dominant in western Amazon Basin.

Corresponding author: Yongjie Huang, Yongjie.Huang@ou.edu; huangynj@gmail.com

Corresponding author: Ming Xue, mxue@ou.edu

Corresponding author: Hector Mayol Novoa, hnovoa@unsa.edu.pe

Abstract

Using the Weather Research and Forecasting (WRF) model with two planetary boundary layer schemes, ACM2 and MYNN, convection-permitting model (CPM) regional climate simulations were conducted for a 6-year period at a 15-km grid spacing covering entire South America and a nested convection-permitting 3-km grid spacing covering the Peruvian central Andes region. These two CPM simulations along with a 4-km simulation covering South America produced by National Center for Atmospheric Research, three gridded global precipitation datasets, and rain gauge data in Peru and Brazil, are used to document the characteristics of precipitation and MCSs in the Peruvian central Andes region. Results show that all km-scale simulations generally capture the spatiotemporal patterns of precipitation and MCSs at both seasonal and diurnal scales, although biases exist in aspects such as precipitation intensity and MCS frequency, size, propagation speed, and associated precipitation intensity. The 3-km simulation using MYNN scheme generally outperforms the other simulations in capturing seasonal and diurnal precipitation over the mountain, while both it and the 4-km simulation demonstrate superior performance in the western Amazon Basin, based on the comparison to the gridded precipitation products and gauge data. Dynamic factors, primarily low-level jet and terrain-induced uplift, are the key drivers for precipitation and MCS genesis along the east slope of the Andes, while thermodynamic factors control the precipitation and MCS activity in the western Amazon Basin and over elevated mountainous regions. The study suggests aspects of the model needing improvement and the choice of better model configurations for future regional climate projections.

Plain Language Summary

We ran high-resolution model simulations at a 3-km grid spacing with two planetary boundary layer schemes (ACM2 and MYNN) for a 6-year period to investigate precipitation and storm patterns in the Peruvian central Andes region. Other datasets including a 4-km simulation produced by National Center for Atmospheric Research, three gridded precipitation products, and rain gauge data in Peru and Brazil were collected for comparison and evaluation. We found that all km-scale simulations capture the overall patterns of precipitation and storms at both seasonal and sub-daily time scales, although some discrepancies exist in precipitation intensity and storm details. Compared to the gridded precipitation products and gauge data, the 3-km simulation using MYNN scheme generally outperforms the other simulations in capturing seasonal and diurnal precipitation over the mountain, while both it and the 4-km simulation demonstrate superior performance in the western Amazon Basin. Low-level wind and terrain-induced uplift is the key driver for precipitation and storm genesis along the Andes' eastern slopes, while factors associated with vertical structures of temperature and humidity control the precipitation and storm activity in the western Amazon Basin and mountain regions. The study suggests aspects of model improvement and better model configurations for future regional climate projections.

1 Introduction

The Peruvian Central Andes, characterized by complex topography and unique climatological conditions such as the South American low-level jet (SALLJ), plays a vital role in influencing local and regional weather patterns and hydrological cycles (Marengo et al., 2002; Vernekar et al., 2003; Vera et al., 2006; Romatschke & Houze Jr, 2010; Drenkhan et al., 2015; Espinoza et al., 2015; Jones, 2019; Poveda et al., 2020; Arias et al., 2021). The precipitation in the Peruvian Central Andes exhibits substantial spatial and temporal variability, driven by multi-scale atmospheric circulations and localized forcing such as topography (Mohr et al., 2014; Junquas et al., 2018; Chavez et al., 2020; Anselmo et al., 2021). Mesoscale convective systems (MCSs), which are organized clusters of thunderstorms, often accompany heavy precipitation, hail, and strong winds (Houze Jr, 2004, 2018; R. S. Schumacher & Rasmussen, 2020). As a major source of precipitation in numerous regions (Salio

et al., 2007; Li et al., 2020; Roca & Fiolleau, 2020; R. S. Schumacher & Rasmussen, 2020; Anselmo et al., 2021; H. Hu et al., 2021; Kukulies et al., 2021; M. Zhao, 2022; Paccini & Stevens, 2023), MCSs can cause severe flooding, landslides, and other natural disasters, thereby posing significant threats to human safety and infrastructure. As shown in Figure 10 of the study by Feng et al. (2021), MCSs can contribute to over 60% of the annual precipitation in the Peruvian Central Andes. Understanding and predicting the behaviors of precipitation and MCSs in the Peruvian Central Andes region are therefore crucial, and understanding the potential impacts of climate change on MCSs is equally important. Research findings in this area can significantly shape water management practices, disaster preparedness, climate change adaptation strategies, and enhance the resilience of local communities and economies to weather-related hazards in a changing climate (Martínez et al., 2008; Vergara et al., 2011; Drenkhan et al., 2015; Gonzalez et al., 2019).

The current understanding of precipitation and MCSs in the Andes and its surrounding regions, however, is limited by the scarcity of public observational databases, especially the scarcity of upper-air radiosonde observations in the region (Condom et al., 2020). State-of-the-art global climate models, such as those participating in the Coupled Model Intercomparison Project Phase 6 (CMIP6) program (Jukes et al., 2020), provide invaluable information on large-scale climate changes over South America. However, limited by available computing resources, the resolutions of these global climate models are too coarse (mostly at grid spacings of ~ 100 km) to resolve local orography and weather phenomena that are important for precipitation production (e.g., MCSs) (Giorgi, 2019; Jukes et al., 2020; Kendon et al., 2021). Numerous studies have highlighted the added value of convection-permitting models (CPMs, typically at a grid spacing of less than 4 km) for simulating precipitation and MCSs in different regions worldwide (A. Prein et al., 2013; Fosser et al., 2015; Sun et al., 2016; Gao et al., 2017; Karki et al., 2017; Liu et al., 2017; Stratton et al., 2018; Zhu et al., 2018; Berthou et al., 2020; Fumière et al., 2020; Guo et al., 2020; Kouadio et al., 2020; Lind et al., 2020; A. F. Prein et al., 2020; Li et al., 2021; Halladay et al., 2023; Paccini & Stevens, 2023). CPMs can significantly improve the representation of land surface conditions including complex topography as well as mesoscale and convective-scale dynamics. Most notably, deep convection can be represented explicitly in CPMs, rather than being parameterized using cumulus schemes which is a major source of uncertainty in quantitative precipitation forecasting.

For example, Sun et al. (2016) found that a 4-km regional climate simulation for the U.S. Great Plains more successfully reproduced the magnitude of extreme precipitation and the diurnal cycle of precipitation than a corresponding 25-km simulation. The 4-km grid also more realistically simulated the low-level jet and related atmospheric circulations important for low-level moisture transport. A. F. Prein et al. (2020) presented a CPM climate simulation over North America at a 4-km grid spacing that was able to capture key characteristics of observed MCSs such as size, precipitation rate, propagation speed, and lifetime, though an underestimate of MCS frequency in the central US during late summer was noted. Paccini and Stevens (2023) demonstrated that simulations at convection-permitting grid spacings (2.5–5.0 km) improved the distribution of precipitation intensity as well as the representation of rainfall diurnal cycle over the Amazon Basin. Better representation of organized convective systems played a key role in improving the precipitation simulations. Halladay et al. (2023) presented a CPM regional climate simulation using the Met Office Unified Model at a 4.5-km resolution for South America covering the period of 1998–2007. They found significant improvements in the representation of precipitation in terms of its diurnal cycle, frequency, and sub-daily intensity distribution. To date, CPM regional climate simulations targeting South America remain limited in number (e.g., V. Schumacher et al., 2020; Bettolli et al., 2021; Lavin-Gullon et al., 2021; Junquas et al., 2022; Dominguez et al., 2023; Halladay et al., 2023; Paccini & Stevens, 2023). Among these, Halladay et al. (2023) and Paccini and Stevens (2023) are the two recent studies over South America covering part of the Peruvian Central Andes region, however, their research is primarily focused on weather

phenomena specific to the Amazonia region. Hence, CPM regional climate simulations and associated research for the Peruvian Central Andes region are still needed.

In light of the lack of long-term reliable observations and insufficient understanding of the role of climate change in precipitation and MCSs in the Peruvian Central Andes region, the present study employs convection-permitting simulations and available precipitation products to probe into the characteristics and mechanisms of precipitation and MCSs in this region. This study will also provide information on the feasibility of using CPM simulations for climate change assessments, particularly in terms of precipitation and MCSs in the Peruvian Central Andes region.

The remainder of this paper is organized as follows: Section 2 describes the datasets employed in this study, along with the model configuration of CPM simulations. In Section 3, the characteristics of precipitation and MCSs are presented and discussed. A summary is offered in Section 4.

2 Data and Method

2.1 Observational data

For the evaluation of simulated precipitation, three global gridded precipitation datasets are utilized: the half-hourly Integrated Multi-satellite Retrievals for GPM (IMERG) at $0.1^\circ \times 0.1^\circ$ resolution (Huffman et al., 2019), the half-hourly NOAA Climate Prediction Center (CPC) MORPHing Technique (CMORPH) with a grid spacing of approximately 8 km (Joyce et al., 2004), and the 3-hourly Multi-Source Weighted-Ensemble Precipitation (MSWEP) version 2, also at $0.1^\circ \times 0.1^\circ$ resolution (Beck et al., 2019). Gauge stations incorporated by IMERG and MSWEP are very sparse in our study region (Huffman et al., 2019; Beck et al., 2019), and CMORPH does not integrate rain gauge data into its precipitation estimates (Joyce et al., 2004). Monthly precipitation data from approximately 400 rain gauge stations in Peru (red dots in Fig. 1, Aybar et al., 2020) are utilized for the evaluation of monthly precipitation. These datasets have been employed in previous simulation evaluations by this research team (Chen et al., 2022; Huang et al., 2023). Additionally, hourly precipitation data from 10 rain gauge stations within the study region, mainly in the western Amazon Basin of Brazil (magenta dots in Fig. 1, accessible at <https://bdmep.inmet.gov.br>), have been collected for the specific evaluation of diurnal cycle of precipitation.

2.2 Model configuration

The simulations conducted in this study utilize the Weather Research and Forecasting (WRF) model with two one-way nested domains, and their configurations are similar to those described by Huang et al. (2023), which are summarized in Table 1. The outer domain (d01) covers the entirety of South America with a horizontal grid spacing of 15 km, and the inner domain (d02) specifically targets the Peruvian central Andes region with a 3-km horizontal grid spacing (Fig. 1). The hourly, 0.25° ECMWF atmospheric reanalysis version 5 (ERA5) data (Hersbach et al., 2020) are used for initial and boundary conditions. Our previous short-term sensitivity tests (Huang et al., 2023) revealed a pronounced sensitivity of simulated precipitation in the Peruvian central Andes region to the choice of planetary boundary layer (PBL) schemes, which can be attributed to differences in free-troposphere mixing in the presence of clouds (X.-M. Hu et al., 2023). We will evaluate whether the performance of CPMs in simulating precipitation and MCSs is similar to our short-term sensitivity study (Huang et al., 2023). Consequently, this study includes two simulations, each employing a different PBL scheme: ACM2 and MYNN level 2.5 based on our previous sensitivity tests (Huang et al., 2023) (Table 1). Limited by computational resources, the simulations cover the period of 2014–2019 with the initial year (2014) serving as the spin-up period, primarily for the land surface model. Hereafter, the two simulations are referred to as WRF3km_ACM2 and WRF3km_MYNN, respectively.

174 Additionally, a simulation with a grid spacing of 4 km, covering the entire South Amer-
 175 ica (Dominguez et al., 2023), produced by the South America Affinity Group (SAAG) led
 176 by National Center for Atmospheric Research (NCAR), is also collected, and the simu-
 177 lation dataset is available at [https://ral.ucar.edu/projects/south-america-affinity-](https://ral.ucar.edu/projects/south-america-affinity-group-saag/model-output)
 178 [group-saag/model-output](https://ral.ucar.edu/projects/south-america-affinity-group-saag/model-output). Hereafter, this dataset is referred to as WRF4km_SAAG. The
 179 WRF4km_SAAG simulation covers a 22-year period (Jan 2000 – Dec 2021) and also uses
 180 0.25° ERA5 reanalysis data for boundary conditions (Dominguez et al., 2023). The main
 181 physics parameterizations used are: YSU PBL scheme (Hong & Lim, 2006), Thompson mi-
 182 crophysics scheme (Thompson et al., 2008), RRTMG radiation scheme (Iacono et al., 2008),
 183 and the Noah-MP land surface model (Niu et al., 2011) with an activated Miguez-Macho-Fan
 184 groundwater scheme (Miguez-Macho et al., 2007; Barlage et al., 2021).

185 To facilitate comparison among the observational and simulated datasets at various res-
 186 olutions, CMORPH, MSWEP, and the simulated fields are regridded to match the IMERG
 187 grid ($0.1^\circ \times 0.1^\circ$) utilizing the “patch recovery” technique, a method previously employed
 188 by Sun et al. (2016) and Huang et al. (2023). The time period analyzed in this study spans
 189 2015 through 2019, encompassing a total of five years.

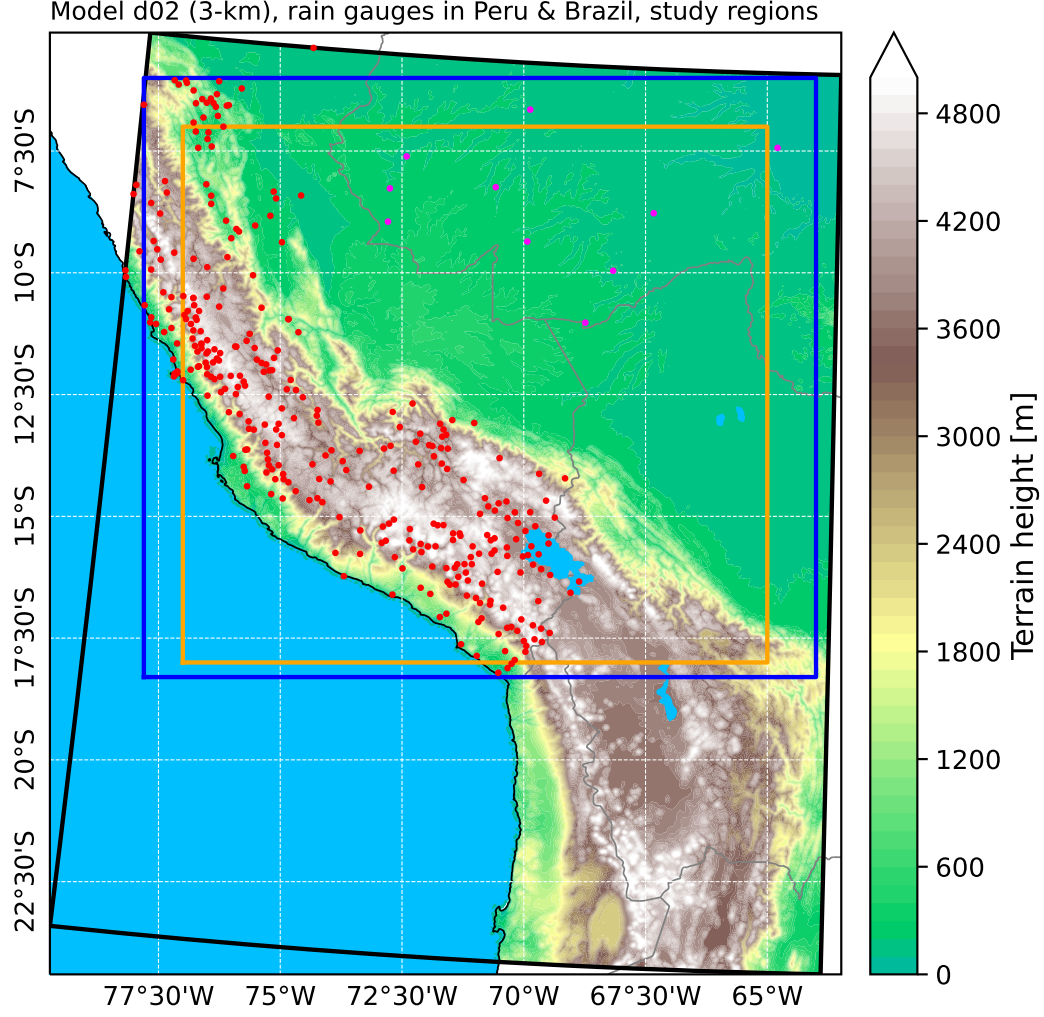


Figure 1. Terrain height (shaded, m) in the 3-km domain with the locations of rain gauges in Peru (red dots) and Brazil (magenta dots). The blue rectangle indicates the region of Figs. 2 and 4. The orange rectangle indicates the region of Figs. 7, 9, 12, and 13.

Table 1. Summary of WRF3km-ACM2 and WRF3km-MYNN^a

	domain 1 (d01)	domain 2 (d02)
Model	WRF V4.2.1 (Skamarock et al., 2019)	
Initial and boundary conditions	ERA5 hourly reanalysis (Hersbach et al., 2020)	
Simulation period	2014–2019 with 2014 as the spin-up period	
Grid spacing	15 km	3 km
Spectral nudging	On (Huang et al., 2023)	Off
Cumulus	Tiedtke (Tiedtke, 1989)	Off
Planetary boundary layer	MYNN level 2.5 (Nakanishi & Niino, 2009) or ACM2 (Pleim, 2007)	
Microphysics	Thompson (Thompson et al., 2008)	
Land surface model	Unified Noah (Ek et al., 2003)	
Surface layer scheme	revised MM5 Monin-Obukhov (Jiménez et al., 2012)	
Longwave and shortwave radiation	RRTMG (Iacono et al., 2008)	

^aMore details can be referred to Huang et al. (2023).

2.3 MCS identification

Python package Tracking and Object-Based Analysis of Clouds (TOBAC, Heikenfeld et al., 2019) is adopted to identify and track MCSs based on the observed and simulated hourly precipitation datasets. In this study, MCSs are identified using a precipitation threshold of 5 mm h^{-1} , which is commonly used in previous studies (Schwartz et al., 2017; A. F. Prein et al., 2017, 2020; Hwang et al., 2023). An object is characterized as a spatially and temporally contiguous precipitation region with a minimum area of 1000 km^2 , approximating a horizontal scale on the order of 100 km (https://glossary.ametsoc.org/wiki/Mesoscale_convective_system). Utilizing the TOBAC output, various MCS characteristics are calculated, including hourly mean precipitation, hourly peak precipitation, hourly precipitation volume, MCS size, duration, and propagation speed.

3 Results

3.1 Precipitation characteristics

Prior to the investigation of MCS characteristics, the simulation of climatological precipitation features such as seasonal and diurnal distributions are evaluated using the three gridded precipitation products in conjunction with rain gauge data.

3.1.1 Seasonal precipitation

In terms of the spatial distribution of seasonally averaged precipitation (Fig. 2), the gridded precipitation products IMERG, CMORPH, and MSWEP show consistent seasonal variations in precipitation distribution, as well as the four notable hotspots along the east slope of the Andes where precipitation can exceed 16 mm day^{-1} in austral summer (December-January-February, DJF). From northeast to southwest, the precipitation exhibits a distinct “strong-weak-strong-weak” spatial pattern. Specifically, it is high over the western Amazon Basin, weakens over the transition between the basin and the foothills of the Andes, increases again along the east slope of the Andes, and then weakens once more over the mountains. The three simulations (Figs. 2d1–f4) successfully reproduce the spatial distributions and seasonal variations of precipitation. The WRF3km_ACM2 simulation, which demonstrated superior performance in precipitation amount in our previous short-term sensitivity experiments (Huang et al., 2023), yields lower precipitation in comparison to the three gridded precipitation products and the other two simulations. This discrepancy is particularly noticeable in the southeastern region of the domain, where the precipitation is less than 6 mm day^{-1} during the summer season (DJF) and less than 3 mm day^{-1} in other seasons (Figs. 2d1–d4). The WRF4km_SAAG simulation exhibits more precipitation compared to the other simulations particularly over the mountainous region, where the precipitation exceeds 6 mm day^{-1} during the summer season (DJF) and is over 3 mm day^{-1} in other seasons (Figs. 2f1–f4). A comparison between the gridded precipitation products, the simulations, and the rain gauge data (primarily located over the mountainous region) confirms the overestimate by WRF4km_SAAG (Fig. 3). Among the three gridded precipitation products compared to the rain gauge data, IMERG has the lowest absolute value of bias (0.16 mm day^{-1}) and root mean square error ($\text{RMSE} = 1.60 \text{ mm day}^{-1}$), and the highest correlation coefficient (0.85) (Fig. 3). Regarding the three simulations, although WRF4km_SAAG has a relatively high correlation with the rain gauge data, with a correlation coefficient of 0.82, it also exhibits the largest bias (1.19 mm day^{-1}) and RMSE (2.53 mm day^{-1}) among all gridded and simulated precipitation data (Fig. 3). Huang et al. (2023) showed that WRF3km_ACM2 simulates monthly precipitation that is the closest to that of the rain gauges in February, 2019, which is also seen in Fig. 3. However, WRF3km_ACM2 underestimates the peaks of monthly precipitation in 2016 and 2017. The monthly precipitation amount of the WRF3km_MYNN simulation falls between WRF4km_SAAG and WRF3km_ACM2, and the correlation coefficient of WRF3km_MYNN with the rain gauge

239 data is 0.79, which is also between those of WRF4km_SAAG (0.82) and WRF3km_ACM2
240 (0.75) (Fig. 3).

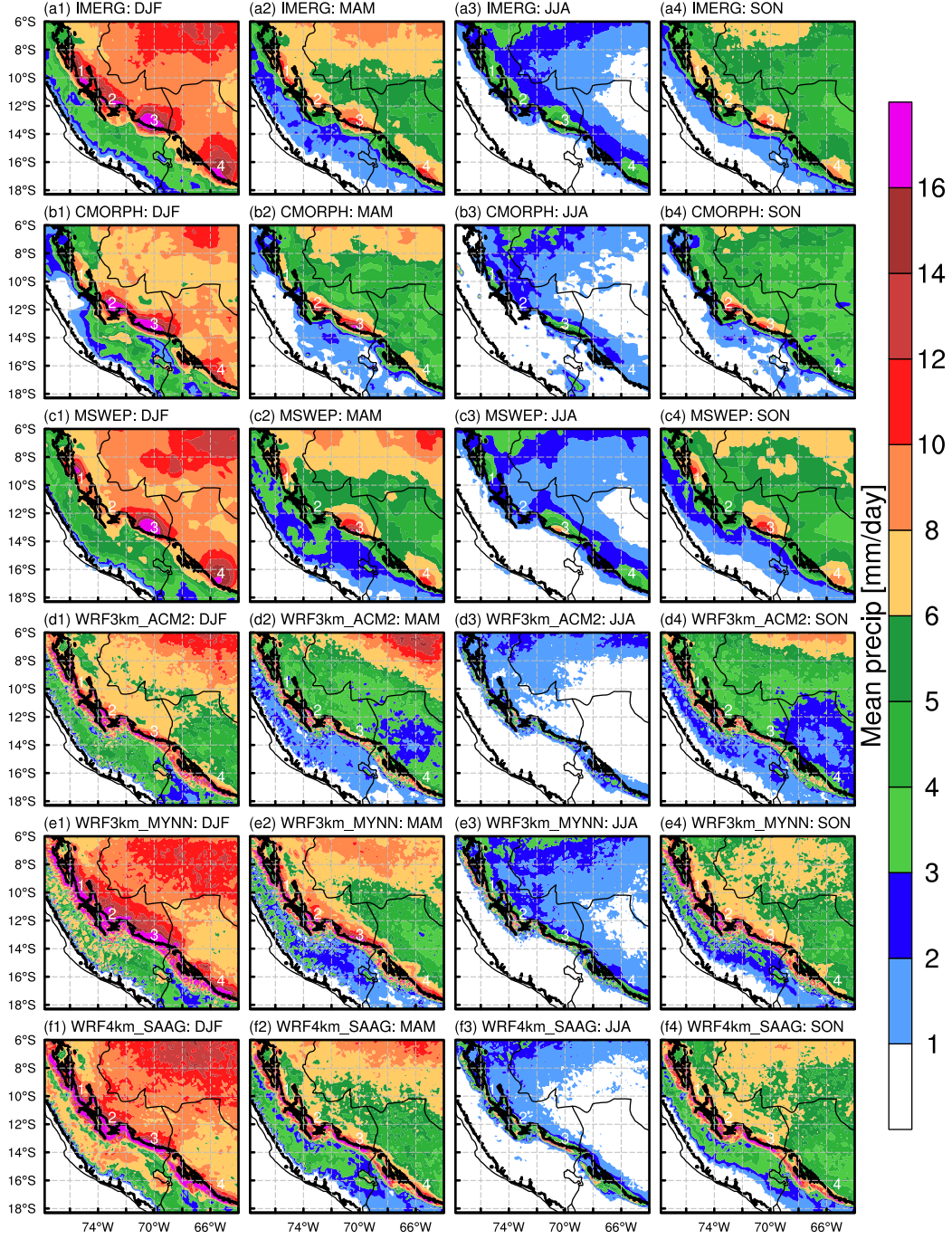


Figure 2. Seasonally averaged precipitation (shaded, mm day^{-1}) for the period of 2015–2019 of (a1–a4) IMERG, (b1–b4) CMORPH, (c1–c4) MSWEP, (d1–d4) WRF3km_ACM2, (e1–e4) WRF3km_MYNN, and (f1–f4) WRF4km_SAAG. (a1–f1) DJF: December-January-February, (a2–f2) MAM: March-April-May, (a3–f3) JJA: June-July-August, and (a4–f4) SON: September-October-November. The black contour in each panel represents 1-km terrain elevation.

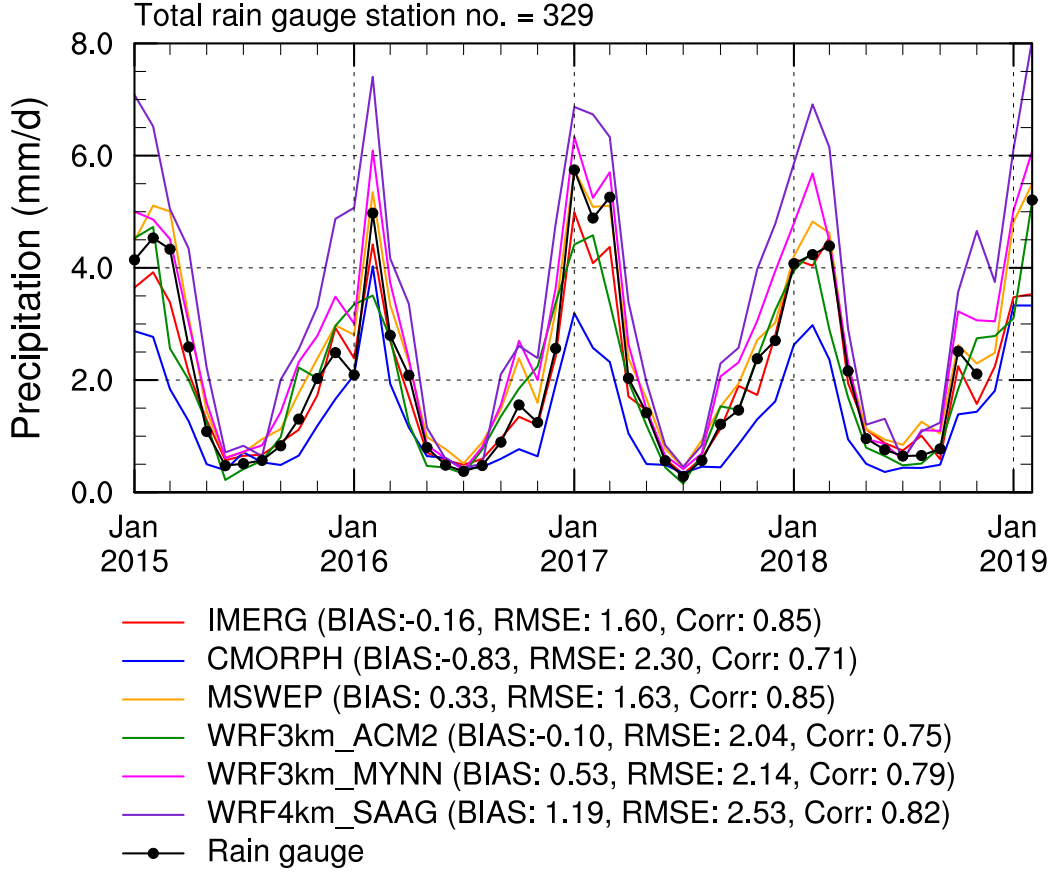


Figure 3. Time series of monthly precipitation (in mm day^{-1}) from rain gauges in Peru within the 3-km domain (Fig. 1), and corresponding data from IMERG, CMORPH, MSWEP, WRF3km_ACM2, WRF3km_MYNN, and WRF4km_SAAG at rain gauge locations. The averaged bias, root mean square error (RMSE), and correlation coefficient between the gridded precipitation products or simulations and the rain gauge data are included in the legend.

Overall, the three simulations broadly capture the spatiotemporal pattern of precipitation at a seasonal scale, but biases in precipitation do exist. Among the simulations of precipitation, WRF3km_MYNN generally outperforms the other two simulations in the Peruvian Central Andes in a combined consideration of bias, RMSE, and correlation coefficient compared with the rain gauge data.

3.1.2 Diurnal cycle of precipitation

The diurnal precipitation peak times of IMERG, CMORPH, and the three simulations are shown in Fig. 4. The MSWEP is not included due to its coarser temporal resolution (three-hourly). As for IMERG and CMORPH, the diurnal precipitation peak time exhibits three distinct belts from the western Amazon Basin to the Andes mountains with a northwest-to-southeast orientation, and this is consistent across all seasons (Figs. 4a1–b4). All three simulations generally reproduce this pattern (Figs. 4c1–e4). While the gridded precipitation products IMERG and CMORPH may have certain biases in precipitation intensity, their diurnal precipitation peak time should be reliable. Using the diurnal precipitation peak time in IMERG as a reference, the seasonal average pattern correlation coefficients with it are 0.900 for CMORPH, 0.856 for WRF3km_ACM2, 0.877 for WRF3km_MYNN, and

0.896 for WRF4km_SAAG. The higher correlation coefficient in WRF4km_SAAG is probably due to its larger model domain at a 4-km grid spacing, while the 3-km WRF runs have a much smaller domain nested within a 15-km grid.

To gain a clearer view of the diurnal precipitation, three regions (represented by blue polygons in Fig. 4) are selected to compute the mean diurnal precipitation over the western Amazon Basin, the Andes foothills, and the mountains, respectively (Fig. 5). Because the spatial distributions of diurnal precipitation peak time are similar across all seasons, only the annual-averaged hourly precipitation as a function of local time is shown in Fig. 5. The precipitation peak time over the western Amazon Basin primarily occurs between ~ 12 – 17 LST (Local Standard Time) with the maximum average precipitation of ~ 0.40 and ~ 0.34 mm h $^{-1}$ in IMERG and CMORPH, respectively (Fig. 5c). The three simulations are able to capture the peak time period in this region. However, in comparison to IMERG, the simulation WRF3km_ACM2 underestimates the average precipitation with a maximum of ~ 0.28 mm h $^{-1}$, while WRF3km_MYNN and WRF4km_SAAG overestimate it with the maximum values of ~ 0.54 and ~ 0.49 mm h $^{-1}$, respectively (Fig. 5c). When compared to the rain gauge data in Brazil (primarily in the western Amazon Basin region, Figs. 1 and 4a), the magnitudes of precipitation in WRF3km_MYNN and WRF4km_SAAG are closer to the rain gauge data than to IMERG (Fig. 6). IMERG actually underestimates the maximum average precipitation by $\sim 20\%$ when compared to the rain gauge data (Fig. 6). Taking the rain gauge data as a reference, the RMSEs for the annual average diurnal precipitation are about 0.054, 0.074, 0.094, 0.051, and 0.037 mm h $^{-1}$ and their corresponding correlation coefficients are around 0.932, 0.891, 0.861, 0.893, and 0.950 for IMERG, CMORPH, WRF3km_ACM2, WRF3km_MYNN, and WRF4km_SAAG, respectively. This suggests that WRF3km_MYNN and especially WRF4km_SAAG perform well in simulating the diurnal cycle of precipitation over the western Amazon Basin with smaller RMSEs and higher correlations. Similarly, the three simulations reproduce the precipitation peak time periods in the foothill and mountain regions, which occur approximately during 0–7 and 13–19 LST, respectively (Fig. 4). Both WRF3km_MYNN and WRF4km_SAAG generally have larger average precipitation in these two regions compared to IMERG, CMORPH, and WRF3km_ACM2 (Figs. 5a and b). Given the lower RMSE for monthly precipitation in WRF3km_MYNN compared to rain gauge data in Peru (Fig. 3), the intensity bias of diurnal precipitation in WRF3km_MYNN should be smaller than that in WRF4km_SAAG over the mountain region. It should be noted that two distinct precipitation peaks are shown in the foothill region (Fig. 5b). This dual-peak pattern is associated with the specific region selected for calculation, which includes the transition zone of precipitation from the Andean foothills to the western Amazon Basin.

Overall, the three simulations successfully capture the spatiotemporal patterns of precipitation at a sub-daily scale, but biases in precipitation amounts are evident. When taking into account both the spatial distribution and intensity of diurnal precipitation, WRF3km_MYNN generally outperforms the other two simulations in the mountain region. Both WRF3km_MYNN and particularly WRF4km_SAAG demonstrate superior performance in the western Amazon region. X.-M. Hu et al. (2023) found that during the morning, the free atmosphere cloud decks dissipate much faster in the simulation using the YSU PBL scheme than the simulation using the ACM2 PBL scheme, leading to more surface radiative heating and convective instability therefore more precipitation in the simulation using the YSU PBL scheme. The cloud cover results in less precipitation in the simulation using the ACM2 PBL scheme.

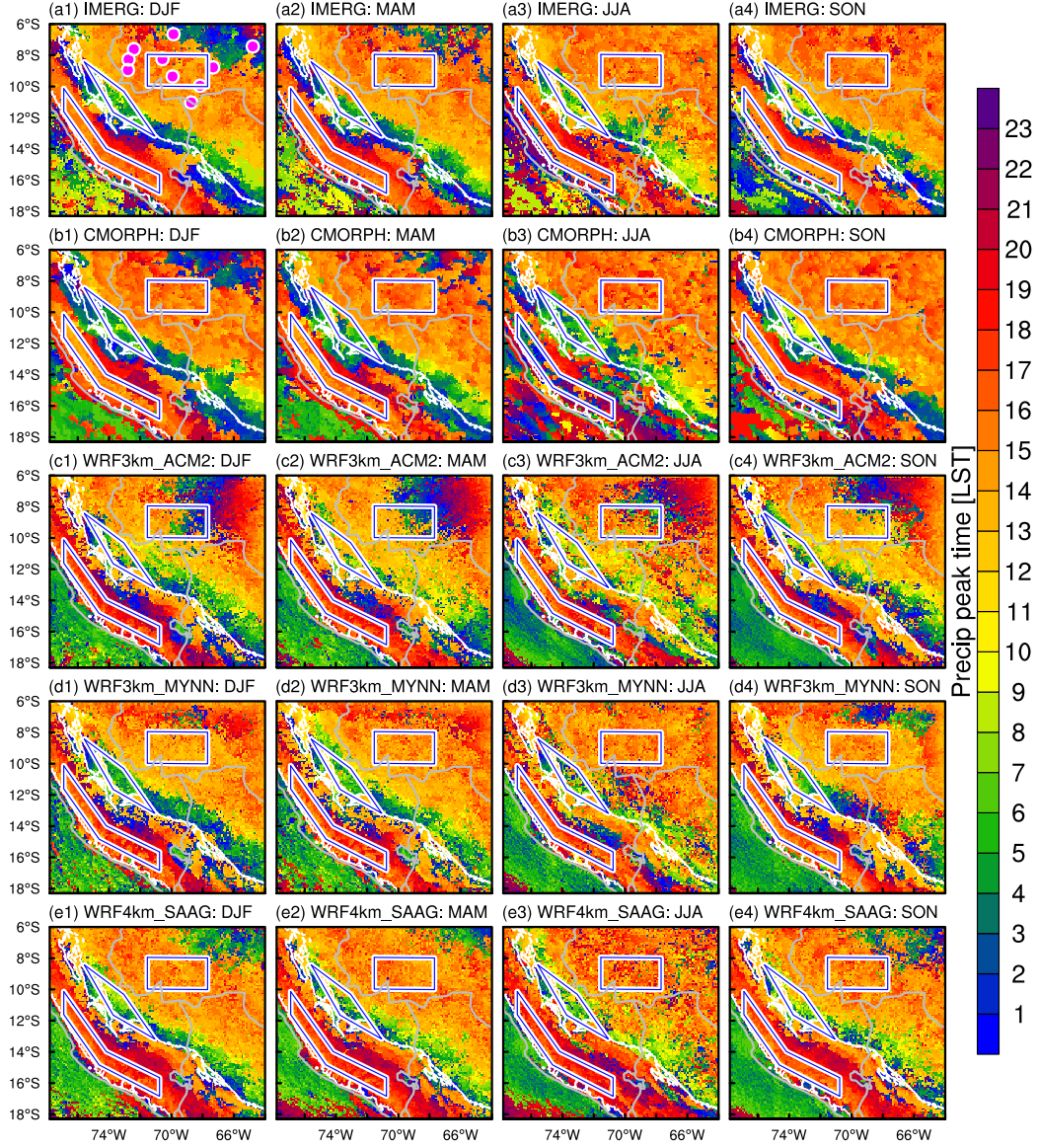


Figure 4. Precipitation peak time (shaded, Local Standard Time, LST) in each season calculated from (a1–a4) IMERG, (b1–b4) CMORPH, (c1–c4) WRF3km_ACM2, (d1–d4) WRF3km_MYNN, and (e1–e4) WRF4km_SAAG. The white contour in each panel represents 1-km terrain elevation. The blue polygons in each panel indicate the regions utilized for diurnal precipitation calculation shown in Fig. 5. The magenta dots in (a1) mark the locations of the hourly rain gauge data in Brazil.

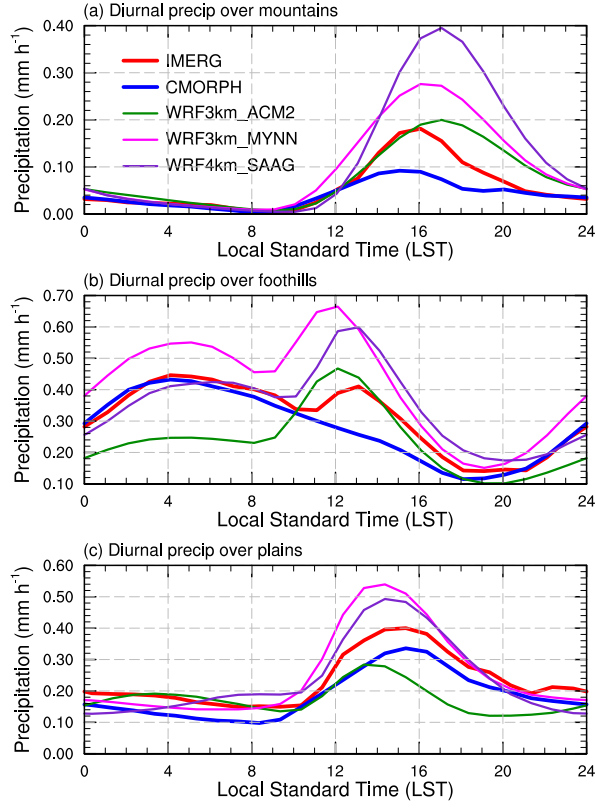


Figure 5. Averaged diurnal precipitation (mm h⁻¹) in the (a) mountain, (b) foothill, and (c) plain regions shown in Fig. 4 from IMERG, CMORPH, WRF3km_ACM2, WRF3km_MYNN, and WRF4km_SAAG.

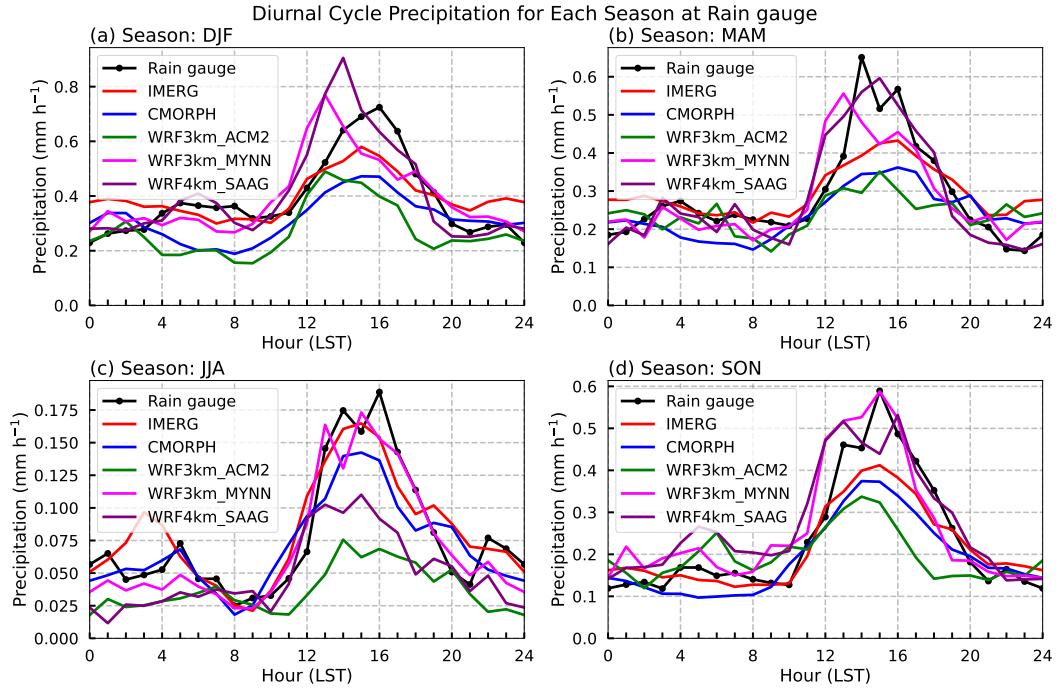


Figure 6. Averaged diurnal precipitation (mm h⁻¹) of rain gauges in Brazil shown in Fig. 4a1 for each season from IMERG, CMORPH, WRF3km_ACM2, WRF3km_MYNN, and WRF4km_SAAG.

3.2 MCS characteristics

The earlier evaluations show that the three WRF simulations effectively reproduce the main features of precipitation at both seasonal and sub-daily time scales in the Peruvian Central Andes region. In the following section, the characteristics of MCSs in this region are examined.

3.2.1 Spatiotemporal distribution and propagation

Only the MCSs generated within the region depicted by the orange rectangle in Fig. 1 are considered. This specified region is smaller than the 3-km simulation domain to reduce the influence of domain boundaries on the analysis. The spatial distributions of seasonal MCS genesis frequency in Fig. 7 reveal that the genesis hotspots for MCSs are along the east slope of the Andes and over the western Amazon Basin. These locations coincide with the precipitation hotspots (Fig. 2), and MCSs can account for up to 50% of annual precipitation in some of these hotspots (not shown), which is also revealed in Feng et al. (2021). All three simulations produce spatiotemporal evolutions of MCSs that are consistent with IMERG and CMORPH, but WRF3km_ACM2 notably underestimates the MCS genesis frequency (Fig. 7). The lower frequency is linked to the underestimate of precipitation in WRF3km_ACM2 (Figs. 2, 3, 5 and 6) and the use of a fixed threshold of 5 mm h^{-1} for MCS identification. The differences in MCS frequency are more apparent in the time series in Fig. 8. Specifically, the MCS frequency in WRF3km_ACM2 is generally lower than in the other datasets, especially during the warm seasons of 2016 and 2019 (Fig. 8a). Conversely, WRF3km_MYNN and WRF4km_SAAG display 5-year average MCS frequencies of about 200 in January and February (Fig. 8b) and the frequency peaks at around 250 in 2019 (Fig. 8a). These two simulations generally exhibit higher MCS frequencies than IMERG and CMORPH during the warm season, exceeding their frequencies by about 20 and 50 ($\sim 10\%$ and $\sim 33\%$) in January and February, respectively (Fig. 8b). However, during the cold season (June and July), WRF3km_MYNN and WRF4km_SAAG simulate about 10 fewer MCSs per month compared to IMERG and CMORPH (Fig. 8b).

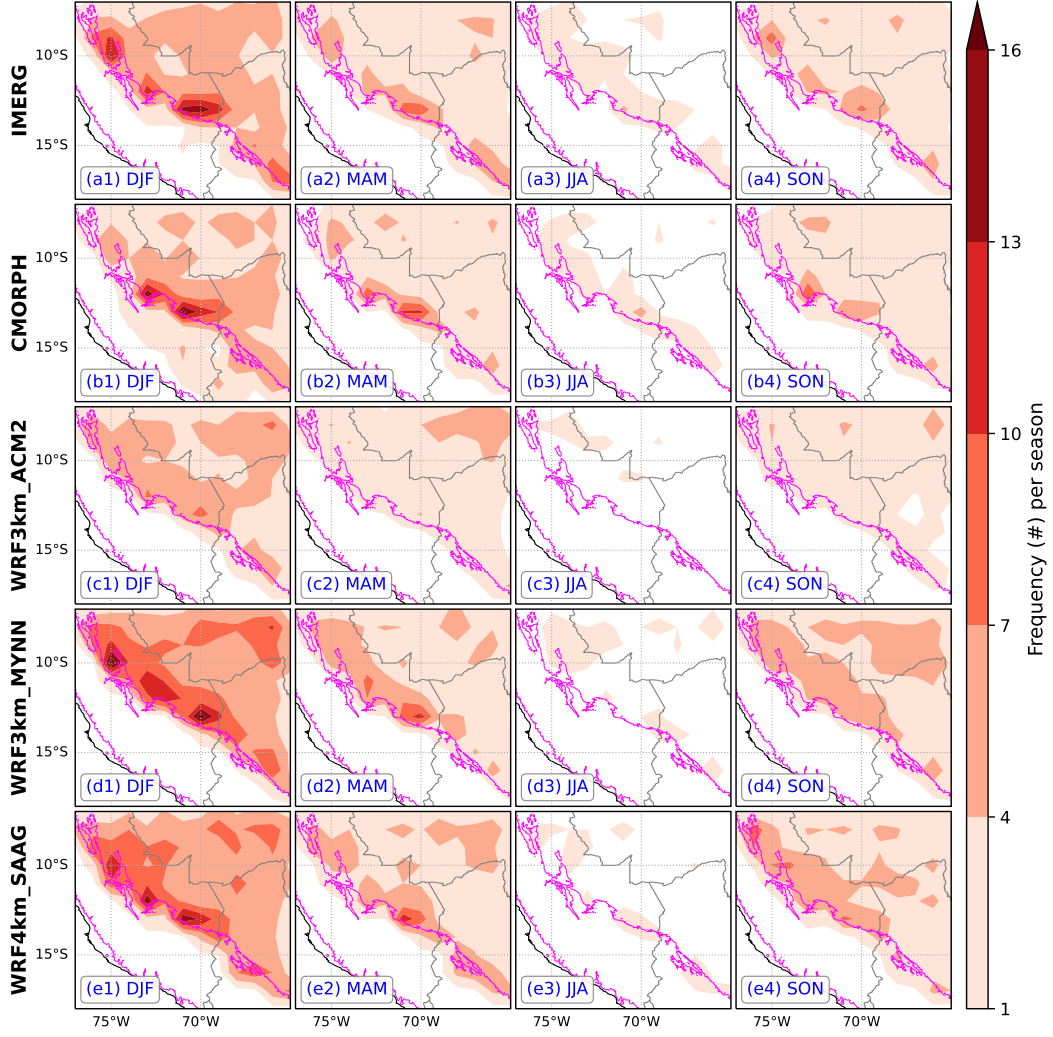


Figure 7. Spatial distribution of MCS genesis frequency (in counts) in $1^\circ \times 1^\circ$ bin in each season for (a1–a4) IMERG, (b1–b4) CMORPH, (c1–c4) WRF3km_ACM2, (d1–d4) WRF3km_MYNN, and (e1–e4) WRF4km_SAG. The magenta contour in each panel represents 1-km terrain elevation.

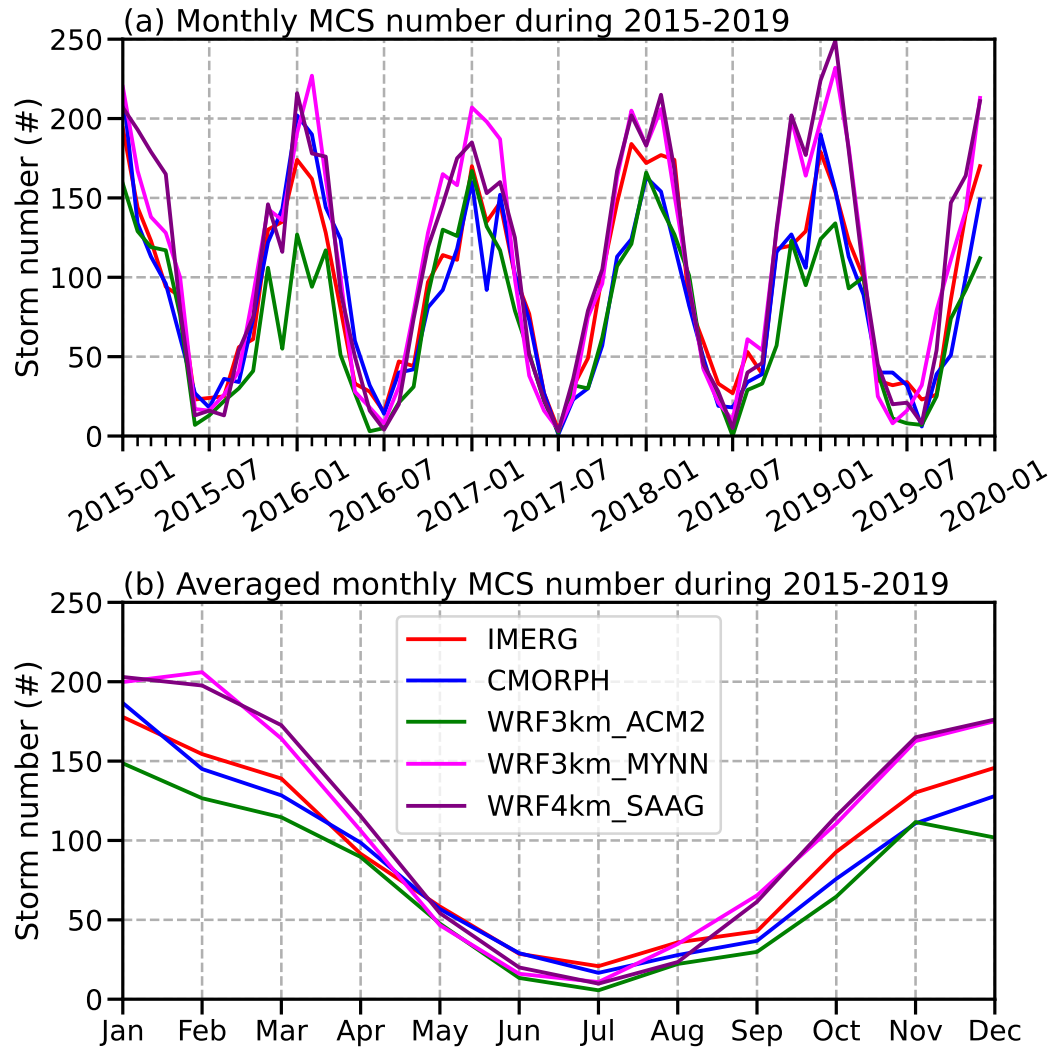


Figure 8. Frequency (in counts) of MCS genesis for (a) each individual month from 2015 to 2019 and (b) the average for each month over the 5-year period for IMERG, CMORPH, WRF3km_ACM2, WRF3km_MYNN, and WRF4km_SAAG.

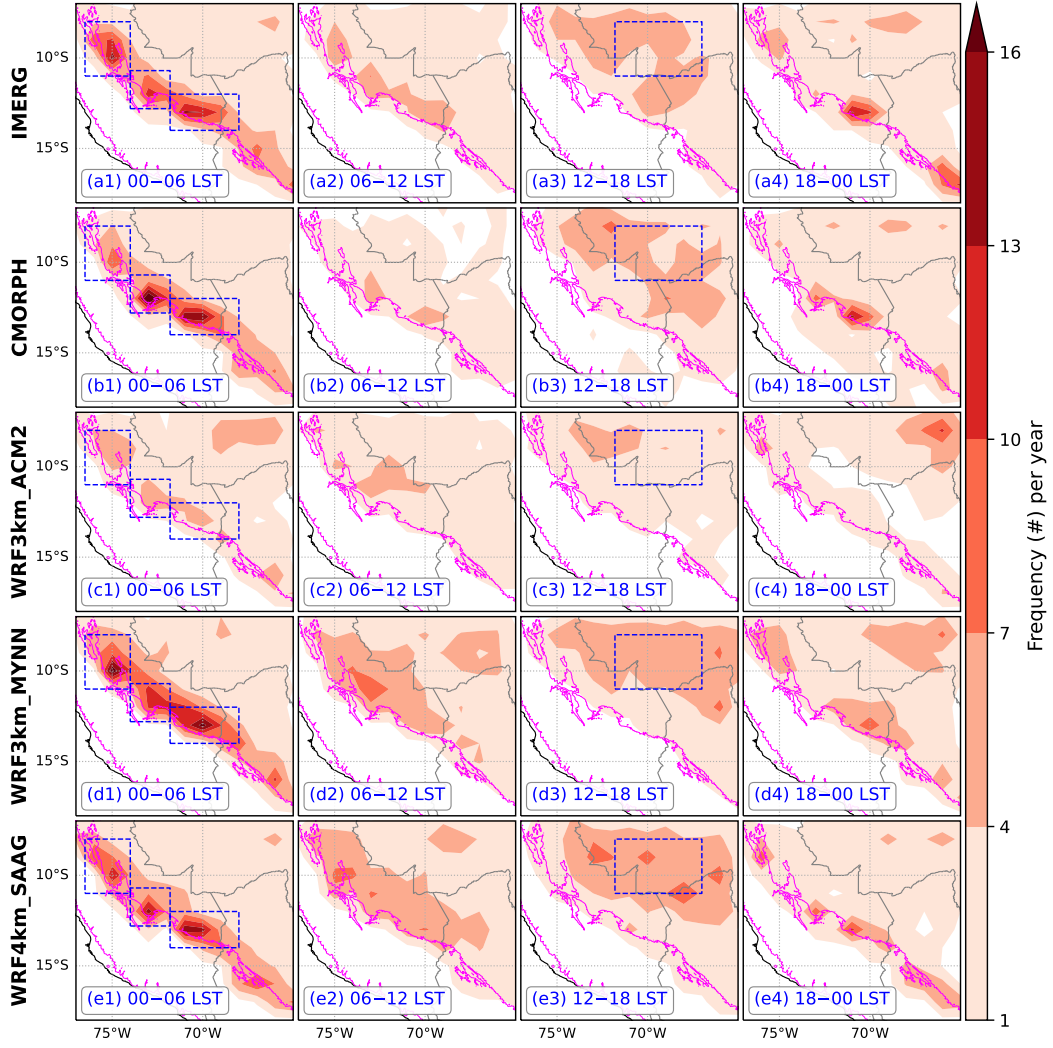


Figure 9. Spatial distribution of the diurnal MCS genesis frequency (in counts) in $1^\circ \times 1^\circ$ bin for (a1–a4) IMERG, (b1–b4) CMORPH, (c1–c4) WRF3km_ACM2, (d1–d4) WRF3km_MYNN, and (e1–e4) WRF4km_SAAAG. The magenta contour in each panel represents 1-km terrain elevation. The Local Standard Time (LST) here is UTC $- 5$ h based on the longitude of 75°W . The blue rectangles in a1–e1 and a3–e3 indicate the regions to create wind roses shown in Fig. 10.

Based on the IMERG and CMORPH data, MCSs along the east slope of the Andes start to initiate during nighttime hours (18–00 LST, see Figs. 9a4 and b4) and reach a peak in genesis frequency in the early morning (00–06 LST, see Figs. 9a1 and b1). In contrast, the western Amazon Basin sees a concentration of MCS genesis in the afternoon (12–18 LST, Figs. 9a3 and b3). All three simulations successfully replicate these diurnal MCS genesis hotspots at terrain notches and over the Amazon Basin. However, WRF3km_ACM2 noticeably underestimates the frequency of MCSs in both the east slope of the Andes and the western Amazon Basin regions (Figs. 9c1–e4).

To examine MCS propagation patterns in the Peruvian Central Andes, MCS propagation direction and speed in the three notable hotspots along the east slope of the Andes and one over the western Amazon Basin are calculated and displayed in the form of wind roses (Fig. 10). It should be noted that the spokes in each wind rose plot indicate the direction towards which MCSs move. The concentric circles in each wind rose plot are divided into 16 sectors at intervals of 22.5° , and each sector would represent a probability of 6.25% if the distribution of MCS propagation were uniform. In observational datasets IMERG and CMORPH, MCSs originating along the Andean east slope mainly propagate parallel to the mountain range (Figs. 10a and b), and the probability of southeastward propagation exceeds 10% in both the northern and southern hotspots in IMERG (Fig. 10a). This behavior likely arises from the natural barrier posed by the high, steep Andean slopes. Over the western Amazon Basin, westward propagation dominates with a probability close to 10% in IMERG data (Fig. 10a), which is close to the motion of downwind-developing MCSs estimated by the method proposed by Corfidi (2003) considering the influence of cold-pool factors (not shown). All three simulations can replicate these dominant MCS propagation characteristics, although discrepancies in specific directional angles, probabilities, and speeds exist (Fig. 10). For instance, WRF3km_ACM2 shows a notably higher northwestward propagation probability both along the east slope of the Andes and over the western Amazon Basin, peaking at probabilities above 15%, a higher value than observed in IMERG (Figs. 10a and c). Northwestward propagation is also prevalent along the east slope of the Andes, as seen in WRF4km_SAAG (Fig. 10e). Compared to WRF3km_ACM2, the WRF4km_SAAG simulation, similar to IMERG (Fig. 10a), exhibits a broader directional spread over the western Amazon Basin, ranging from southward to northwestward, with the highest probability of $\sim 10\%$ in the west-northwestward direction (Fig. 10e). WRF3km_MYNN closely aligns with IMERG for MCS propagation along the Andean slope but veers more southward over the Amazon Basin (Fig. 10d). Additionally, all three simulations simulate higher probabilities for MCS propagation speeds exceeding 65 km h^{-1} compared to IMERG and CMORPH, implying an overestimate of MCS propagation speed in the simulations. However, it should be noted that IMERG and CMORPH also have uncertainties, especially in CMORPH, whose MCS propagation direction has a large difference from IMERG and all simulations (Fig. 10).

Overall, although specific discrepancies exist in the MCS genesis frequency and propagation speed, the WRF simulations generally replicate the observed spatiotemporal patterns at both seasonal and diurnal scales and the propagation of MCSs in the Peruvian Central Andes and western Amazon.

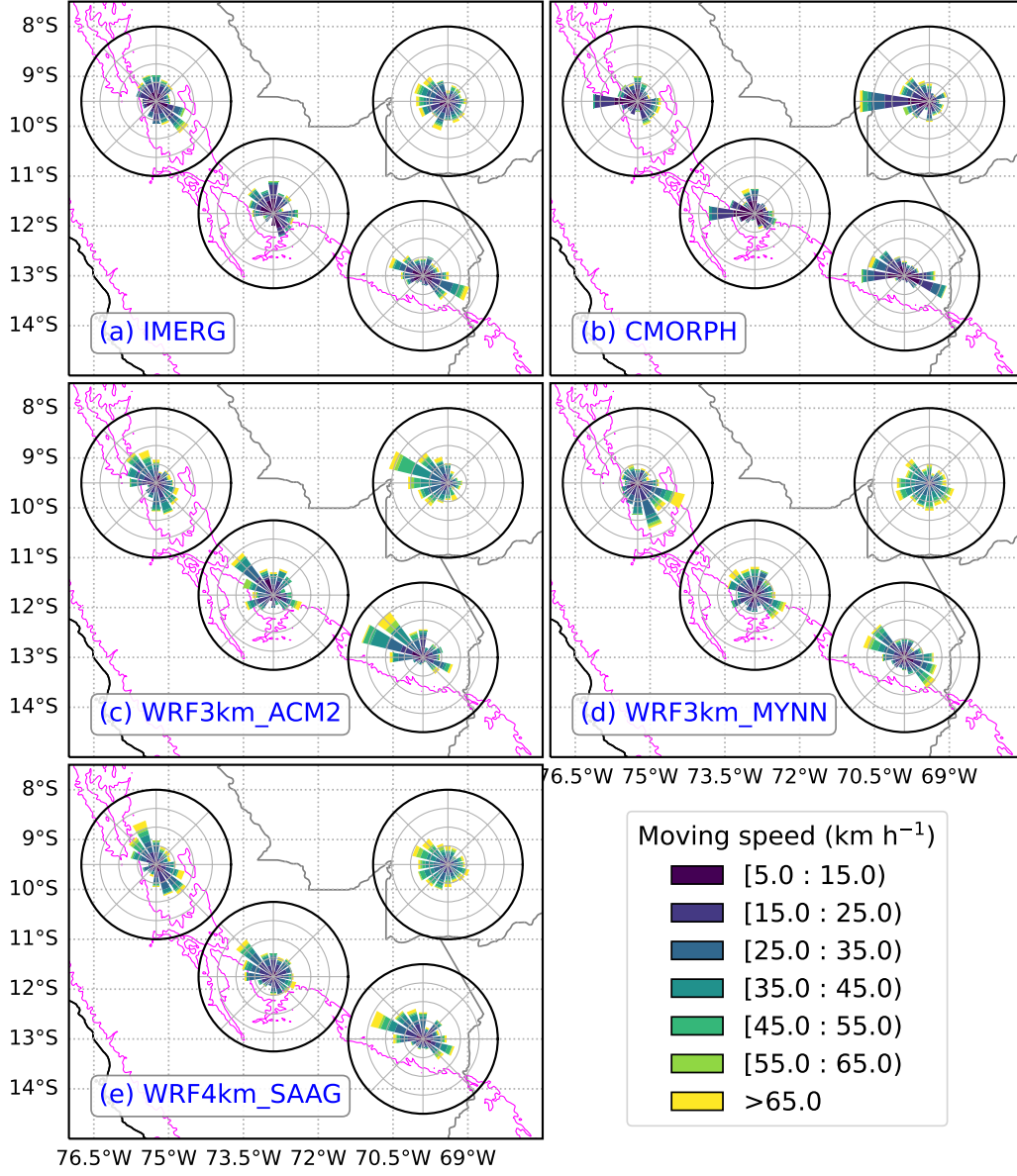


Figure 10. Wind roses for MCS propagation in the hotspots along the east slope of the Andes and in the western Amazon Basin shown in Fig. 9 for (a) IMERG, (b) CMORPH, (c) WRF3km_ACM2, (d) WRF3km_MYNN, and (e) WRF4km_SAAG. The concentric circles in each panel indicate the probability (5, 10, 15, and 20%) of propagation direction, divided into 16 sectors at intervals of 22.5°. The colors within the circles represent the MCS moving speed classes, segmented into intervals of 10 km h⁻¹. The magenta contour in each panel represents the 1-km terrain elevation.

3.2.2 Statistics of MCS properties

In this section, MCS properties are statistically examined to identify main differences in MCSs among IMERG, CMORPH and all simulations. Properties of MCSs, such as hourly mean precipitation, peak hourly precipitation, size, duration, hourly precipitation volume (equals hourly mean precipitation \times area), and moving speed, are displayed for IMERG, CMORPH, WRF3km_ACM2, WRF3km_MYNN, and WRF4km_SAAG using violin plots (Fig. 11). The MCS properties are generally consistent between IMERG and CMORPH, as well as among the three simulations themselves, as shown in Fig. 11. However, a significant discrepancy exists between the gridded precipitation products, IMERG and CMORPH, and the simulations, WRF3km_ACM2, WRF3km_MYNN, and WRF4km_SAAG, particularly in MCS precipitation intensity, including both mean and peak hourly precipitation (Figs. 11a and b). The interquartile range (25th to 75th percentiles) for the mean hourly precipitation in IMERG and CMORPH spans $\sim 8\text{--}11\text{ mm h}^{-1}$, centering around a median value of $\sim 9\text{ mm h}^{-1}$. In contrast, all simulations exhibit a higher interquartile range, covering $\sim 13\text{--}19\text{ mm h}^{-1}$, and center around median values of about 16 mm h^{-1} (Fig. 11a). The differences between the gridded precipitation products and simulations are also evident in peak hourly precipitation rates. Specifically, the 25th, 50th (median), and 75th percentiles for IMERG are approximately 14, 20, and 28 mm h^{-1} , respectively, and for CMORPH, they are around 14, 18, and 24 mm h^{-1} . In contrast, these percentiles are notably higher in the simulations: for WRF3km_ACM2, they are about 35, 46, and 59 mm h^{-1} ; for WRF3km_MYNN, they are approximately 38, 48, and 60 mm h^{-1} ; and for WRF4km_SAAG, the values are around 40, 51, and 64 mm h^{-1} (Fig. 11b). This suggests that the simulations tend to overestimate the median of peak hourly precipitation by more than 130% compared to the IMERG. Regarding MCS size, IMERG and CMORPH show 25th to 75th percentile ranges of approximately 4700 to 12000 km^2 , with median sizes close to 7000 km^2 (Fig. 11c). However, the simulations generally produce smaller MCS sizes, with 25th to 75th percentile ranges spanning about 3000 to 7000 km^2 and median sizes around 4000 km^2 . Despite the smaller sizes, the simulations exhibit higher precipitation intensity (Fig. 11a). Consequently, the simulated and observed hourly precipitation volumes are relatively similar (Fig. 11e). Specifically, the 25th to 75th percentile ranges in the simulated and observed hourly precipitation volumes are approximately 0.04 to $0.11\text{ km}^3\text{ h}^{-1}$, with median volumes of around $0.065\text{ km}^3\text{ h}^{-1}$ (Fig. 11e). Meanwhile, all datasets exhibit a median MCS duration of 3 hours (Fig. 11d). However, the simulations generally produce higher MCS movement speeds, with a median of $\sim 36\text{ km h}^{-1}$, compared to the observed median speeds of $\sim 20\text{ km h}^{-1}$ in IMERG and CMORPH (Fig. 11f), which aligns with the findings presented in Fig. 10.

Overall, statistical analyses of MCS properties reveal that the simulations generally overestimate both mean and peak hourly precipitation rates associated with MCSs, and simulate smaller MCS sizes but similar hourly precipitation volumes compared to gridded precipitation products. All datasets agree on a median MCS duration of 3 hours, though simulated MCSs tend to move faster. It should be noted that the discrepancies between the simulations and the gridded precipitation products may also arise from the uncertainties and low effective resolutions of the gridded precipitation products (Guilloteau & Foufoula-Georgiou, 2020), thereby emphasizing the need for more reliable observational products.

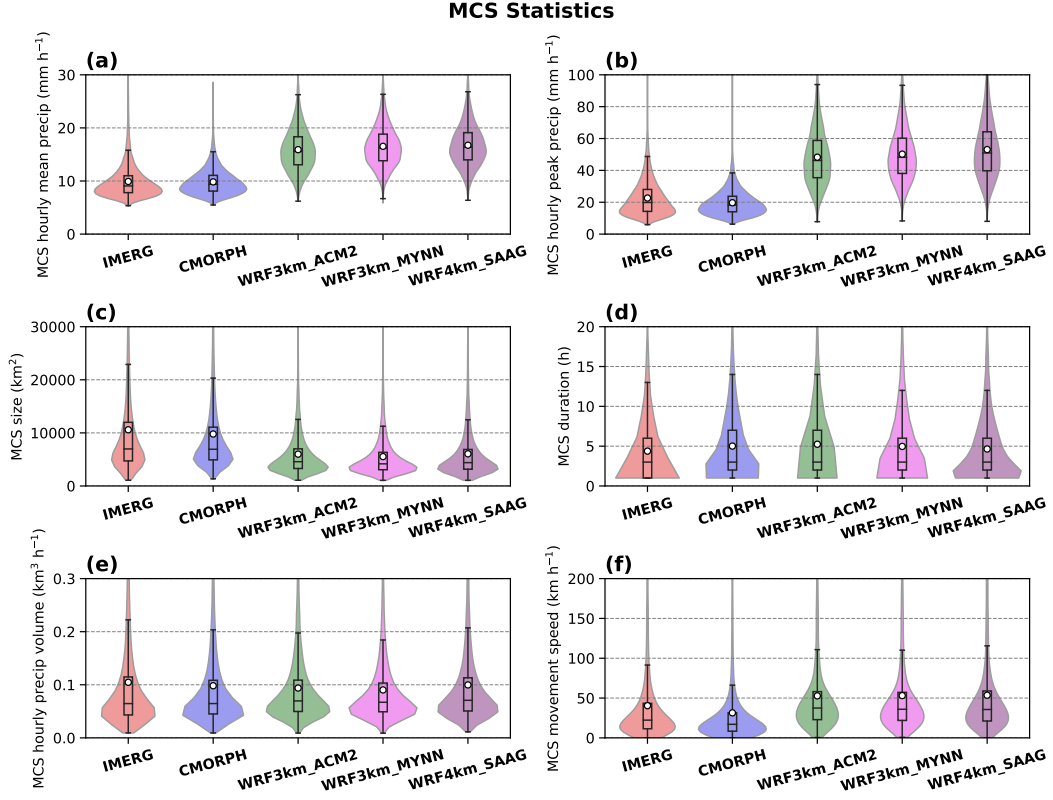


Figure 11. Violin plot of MCS properties including MCS (a) hourly mean precipitation, (b) hourly peak precipitation, (c) size, (d) duration, (e) hourly precipitation volume, and (f) moving speed for IMERG, CMORPH, WRF3km_ACM2, WRF3km_MYNN, and WRF4km_SAAG. The white circles in box-and-whisker plots represent the average value of samples. The distributions and medians of the gridded precipitation products and simulations are significantly different at the 0.05 level, except for MCS duration comparisons between CMORPH and WRF3km_ACM2 or WRF3km_MYNN.

3.2.3 Diurnal dynamic and thermodynamic factors

Despite noted differences in MCS precipitation intensity, frequency, and movement speed, all three simulations, particularly WRF3km_MYNN, successfully replicate key spatiotemporal distributions and evolution of MCSs across multiple scales. In the subsequent section, diurnal variations of dynamic and thermodynamic fields from the 3-km simulations WRF3km_MYNN and WRF3km_ACM2 are used to understand the mechanisms underlying MCS genesis in this region.

From the DJF-seasonal mean hourly horizontal wind fields at 850 hPa in WRF3km_MYNN and WRF3km_ACM2 shown in Figs. 12 and 13, we can see that the mean winds in the examined region on the east of the Andes are predominantly northwesterly, influenced mainly by the steep high Andean terrain that blocks the northeasterly SALLJ and turns the flows into northwesterly. However, the mean wind speed in WRF3km_MYNN ($\sim 3.9 \text{ m s}^{-1}$) is closer to that in ERA5 ($\sim 4.6 \text{ m s}^{-1}$, not shown) than that in WRF3km_ACM2 ($\sim 2.6 \text{ m s}^{-1}$). In WRF3km_MYNN, wind convergence (divergence $< -1 \times 10^{-6} \text{ s}^{-1}$) is primarily found along the east slope of the Andes and over the western Amazon Basin between 00–06 LST (Figs. 12a–g). Such enhancement of convergence and precipitation in the early morn-

ing hours near the LLJ terminus (Fig. 14a) can be mostly explained by the boundary layer inertial oscillation theory (Blackadar, 1957; Xue et al., 2018).

Starting from 07 LST, the convergence zones begin to contract and become concentrated within the basin area around the latitude of 10° S between 12–15 LST (Figs. 12h–p). From 16 LST, convergence gradually expands and eventually covers both the Andean slope and the basin regions again (Figs. 12q–x). Such distribution and evolution of wind convergence in WRF3km_MYNN are consistent with those in ERA5 (not shown). The diurnal variations in wind convergence and horizontal wind speeds along the east slope of the Andes (Figs. 12 and 14a) are consistent with the diurnal variation of MCS genesis in the region, where the frequency of MCSs begins to increase between 18–00 LST and peaks between 00–06 LST (Fig. 9). This suggests that MCS activity and precipitation along the eastern Andean slope are mainly driven by dynamical forcings, such as the uplift of moist air by SALLJ and by the mountain-range-parallel northwesterly flows when they encounter the terrain notches near the precipitation hotspots. In WRF3km_ACM2 (Fig. 13), the area of the wind convergence (divergence $< -1 \times 10^{-6} \text{ s}^{-1}$) first decreases and then increases from 00 to 23 LST, which is consistent with that in WRF3km_MYNN. However, in WRF3km_ACM2 (Fig. 13), the wind convergence (divergence $< -1 \times 10^{-6} \text{ s}^{-1}$) primarily covers the east slope of the Andes and part of the western Amazon Basin between 00–06 LST (Figs. 13a–g). The horizontal wind speeds associated with LLJ are also weaker in WRF3km_ACM2 than in WRF3km_MYNN (Fig. 14). There are few convergence zones in the study region between 12–15 LST (Figs. 13h–p). It is consistent with the weaker precipitation ((Figs. 2, 5, and 6) and fewer MCS geneses (Fig. 9) over the western Amazon Basin in WRF3km_ACM2.

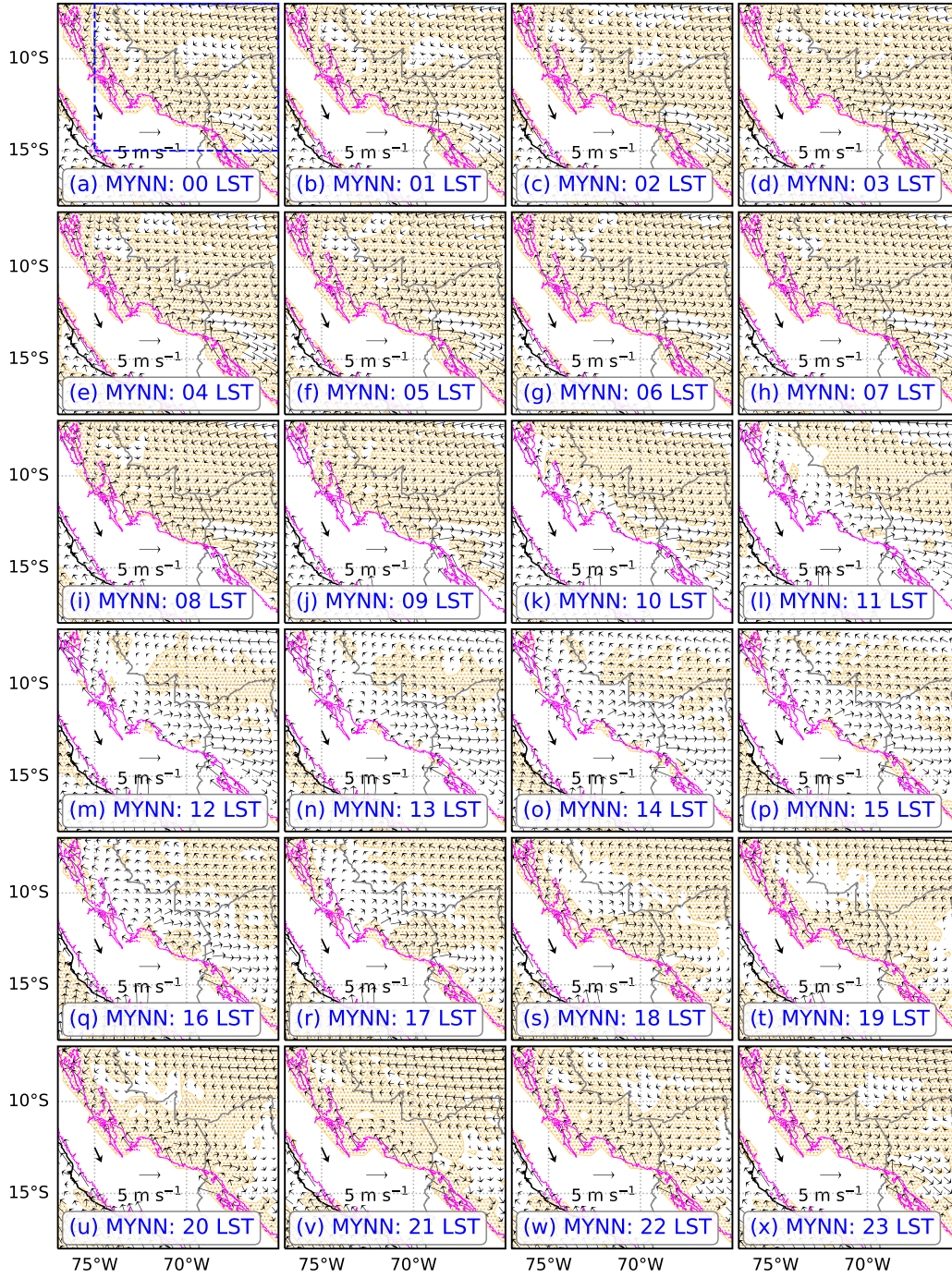


Figure 12. Diurnal horizontal winds at 850 hPa averaged over the DJF months from 2015 to 2019 in WRF3km.MYNN. In order to see the convergence region clearly, the full wind field is decomposed into two components: Thick vectors represent the time-area-averaged wind in the blue dashed box shown in (a), and thin vectors represent the deviation of the full wind field from the time-area-averaged wind. The orange dot-filled areas indicate the regions with wind divergence less than $-1 \times 10^{-6} \text{ s}^{-1}$. The magenta contour in each panel represents 1-km terrain elevation. The Local Standard Time (LST) here is UTC $- 5 \text{ h}$ based on the longitude of 75°W .

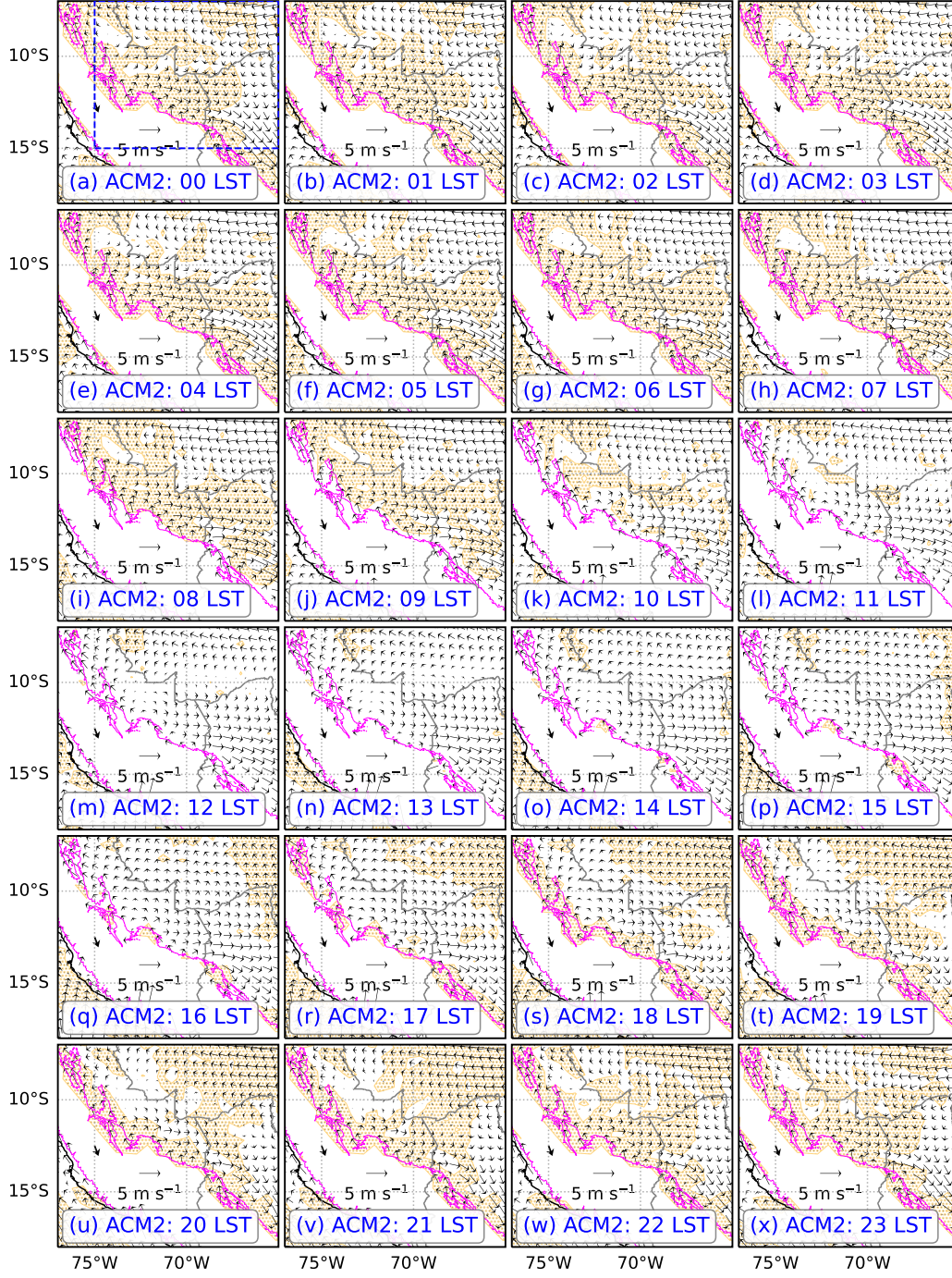


Figure 13. As in Fig. 12, but for WRF3km.ACM2.

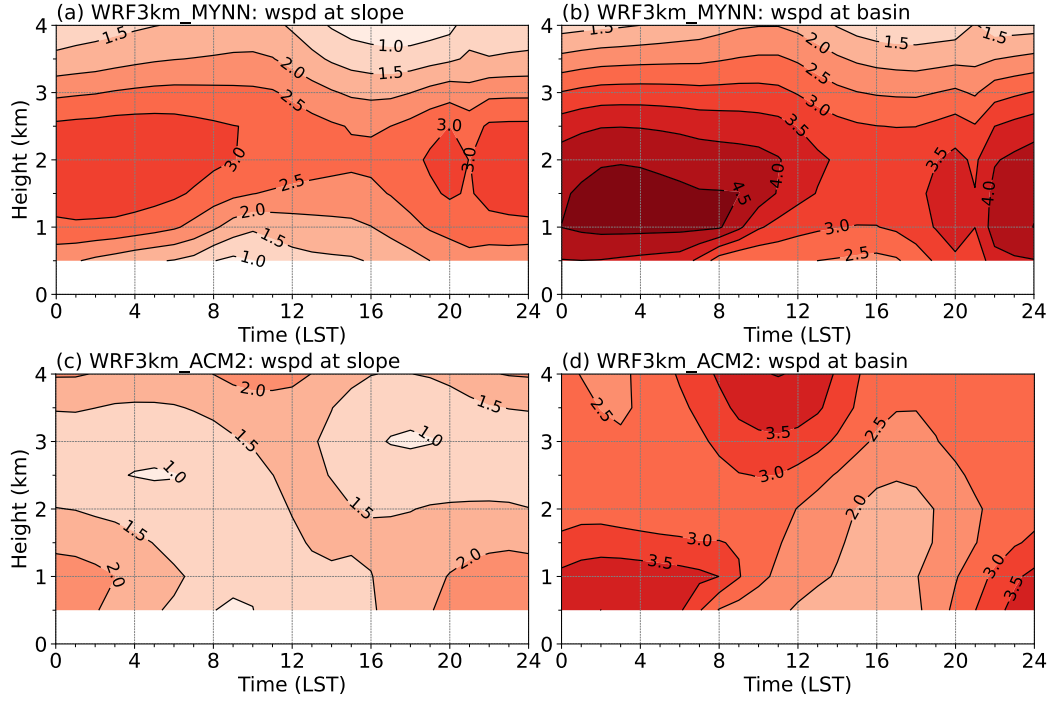


Figure 14. Height-time cross-section of area-averaged horizontal wind speeds (m s^{-1}) in the regions of (a and c) northern MCS genesis hotspot along the east slope of the Andes and (b and d) the hotspot over the western Amazon Basin (blue rectangles shown in Fig. 9) in (a and b) WRF3km_MYNN and (c and d) WRF3km_ACM2, respectively.

For the western Amazon Basin, convergence is consistently present throughout the day in WRF3km_MYNN (Fig. 12) and ERA5 (not shown). Despite this, MCSs predominantly form between 12–18 LST (Fig. 9), indicating that dynamic convergence associated with low-level flows is not the most dominant driver of MCS activity in this region. Thermodynamic forcing likely plays even more important roles in triggering and supporting a majority of MCSs. To further understand the underlying mechanisms, vertical cross-sections of diurnal vertical velocity at the latitude of 10° S are examined, along with maximum convective available potential energy (CAPE) and maximum convective inhibition (CIN) (Figs. 15 and 16).

In WRF3km_MYNN, during the early morning hours (00–06 LST), strong updrafts are observed on the Andean east slope, mainly attributed to enhanced low-level flows (Fig. 14a) and associated terrain lifting, although the CAPE values are moderate, ranging from approximately 500 to 1000 J kg⁻¹ (Figs. 15a–g). In the western Amazon Basin, CAPE is comparable, but CIN is noticeably higher (up to ~160 J kg⁻¹) (Figs. 15a–g), inhibiting the triggering of significant convection despite the convergence. Starting at 07 LST, both CAPE and CIN undergo diurnal changes in the basin due to solar radiative heating. CAPE rises to 1200–1600 J kg⁻¹, while CIN approaches zero between 10–15 LST (Figs. 15h–p). Consequently, updraft frequency in the basin increases during this period. During 11–13 LST (Figs. 15l–n), updrafts shift from the Andean slope to the smaller mountains to the east (around 74°W) with a low CAPE between 400–800 J kg⁻¹, showing the importance of even small terrains here. In contrast, despite maximum CAPE values on the Andean slopes up to 1600 J kg⁻¹ (Figs. 15n–p), updrafts in this region decline, which is largely attributed to divergence in this region associated with enhanced convection upstream over the basin (Figs. 12k–p). Although CAPE starts to decrease and CIN begins to rise after 16 LST, updrafts can persist for a while due to the presence of existing convection and relatively high prior CAPE (> 800 J kg⁻¹, Figs. 15q–u) and previous convection trigger effect. Hence, MCSs in the western Amazon Basin are predominantly influenced by thermodynamic factors. Additionally, updrafts are observed at elevations around 4 km during 12–18 LST over the mountains, aligning with the evolution of CAPE and precipitation in the regions (Figs. 15m–s and Fig. 5a). It suggests that thermodynamic factors also have a significant influence on precipitation over these elevated terrains. In fact, over major mountain ranges, afternoon convection is often prevalent, such as over the Rocky Mountains (e.g., Carbone & Tuttle, 2008; Sun et al., 2016; Y. Zhao et al., 2023).

For the WRF3km_ACM2 simulation (Fig. 16), the diurnal evolution of updrafts, CAPE and CIN are basically consistent with those in WRF3km_MYNN (Fig. 15). However, there exist obvious differences in their magnitudes. From 00 to 07 LST, CAPE in WRF3km_ACM2 is around 400 J kg⁻¹ (Figs. 16a–h), which is ~100–500 J kg⁻¹ smaller than that of WRF3km_MYNN (Figs. 15a–h). In the meanwhile, CIN in WRF3km_ACM2 is mostly between 80 and 160 J kg⁻¹ and can be up to 200 J kg⁻¹ over the western Amazon Basin, which is about 40 J kg⁻¹ higher than that of WRF3km_MYNN (Figs. 16a–h and 15a–h). Therefore, the triggering of updrafts is more inhibited in WRF3km_ACM2, which is consistent with the weaker updrafts in WRF3km_ACM2. Between 08–15 LST, CAPE in WRF3km_ACM2 starts to increase, but it is lower than 1200 J kg⁻¹ and mostly around 800 J kg⁻¹ over the western Amazon Basin (Figs. 16i–p), about 400 J kg⁻¹ smaller than that in WRF3km_MYNN (Figs. 15i–p). Moreover, CIN is also generally higher in WRF3km_ACM2 than in WRF3km_MYNN in this period. Thus, there are much fewer updrafts over the western Amazon Basin in WRF3km_ACM2 (Figs. 16i–p). Therefore, the lower CAPE and higher CIN along with the weaker LLJ and fewer convergence zones in WRF3km_ACM2 result in weaker precipitation and fewer MCSs than WRF3km_MYNN. These differences were also found in our previous short-term simulation study (Huang et al., 2023), and analyses in X.-M. Hu et al. (2023) show that the differences in the strength of vertical mixing within the PBL and entrainment flux at the PBL top in different PBL schemes impact the vertical transportation of moisture and momentum. This affects cloud formation and cloud fraction, ultimately influencing surface radiative heating, CAPE and precipitation (Huang et

508 al., 2023; X.-M. Hu et al., 2023). Sensitivity experiments in X.-M. Hu et al. (2023) suggest
509 that the stronger free-troposphere mixing in ACM2 scheme is the primary factor responsible
510 for the discrepancies in the vertical thermodynamic structure and simulated precipitation
511 between the simulations using different PBL schemes.

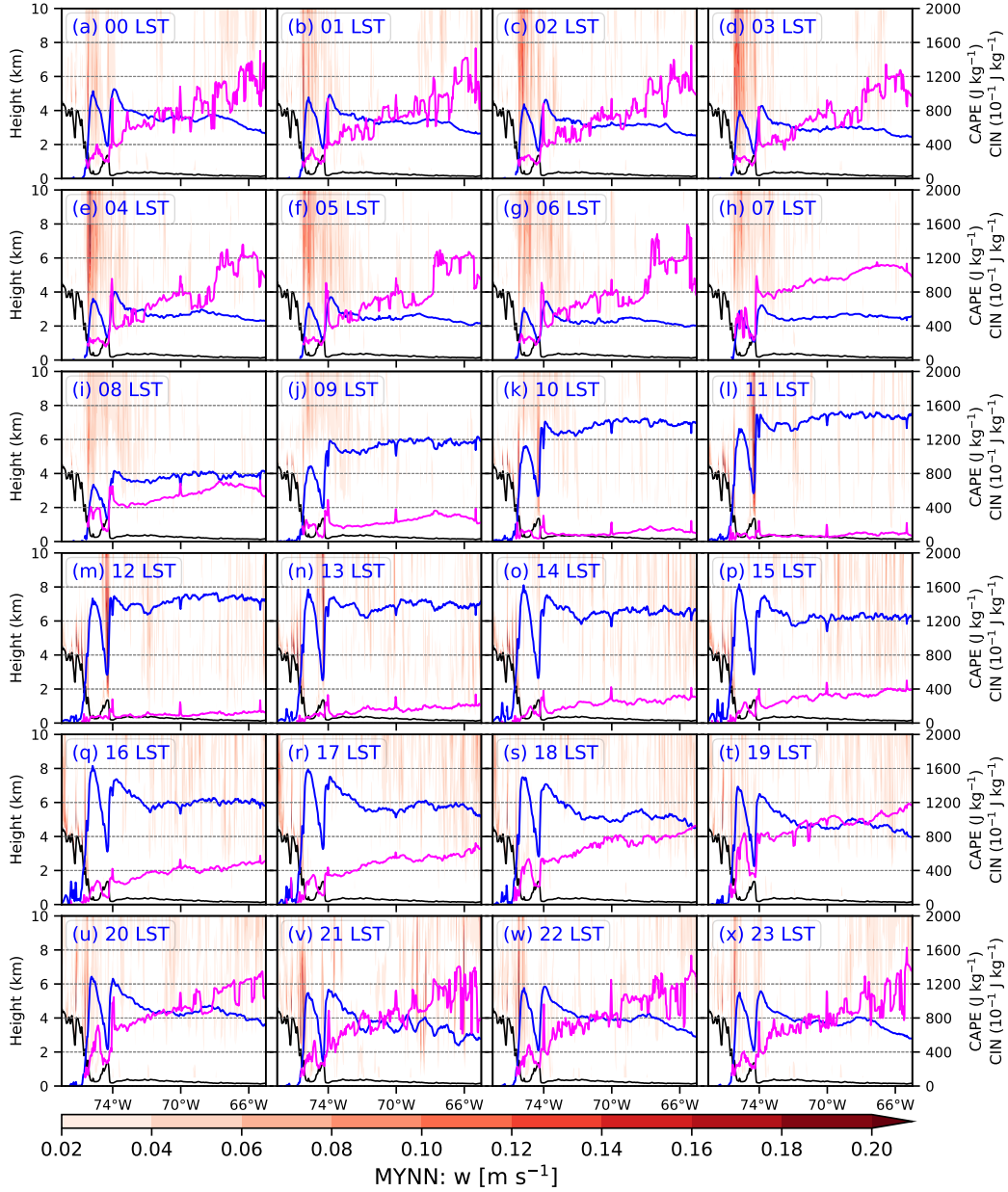


Figure 15. Vertical cross-section of vertical velocity (shaded, in units of m s^{-1}) along the latitude of 10°S in WRF3km.MYNN. The black curves represent the terrain height (km), and the blue and magenta curves represent CAPE (J kg^{-1}) and CIN ($10^{-1} \text{ J kg}^{-1}$), respectively. The unit of CIN in $10^{-1} \text{ J kg}^{-1}$ is used here to make CIN more visible. The Local Standard Time (LST) here is UTC - 5 h based on the longitude of 75°W .

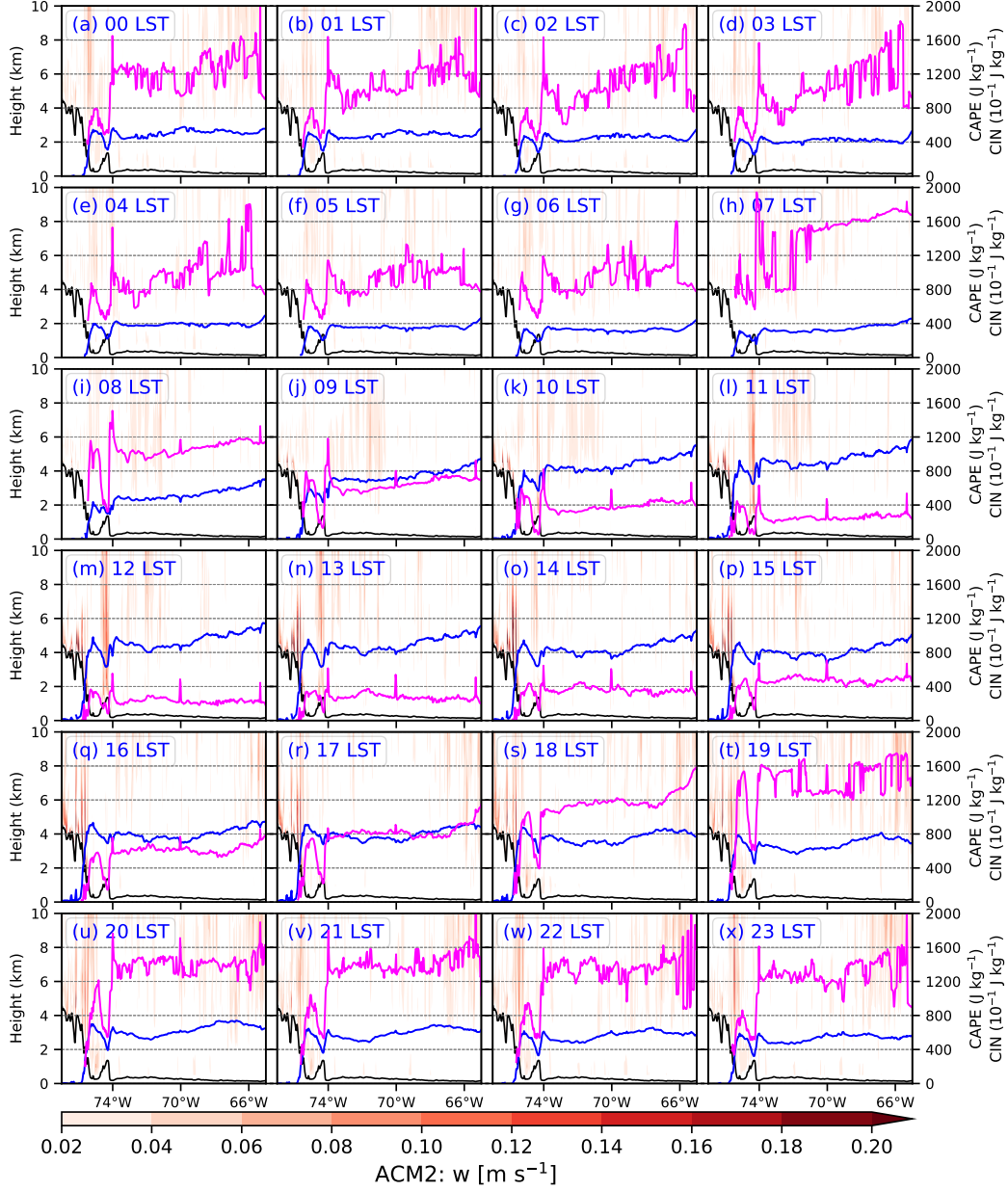


Figure 16. As in Fig. 15, but for WRF3km.ACM2.

4 Summary

To investigate the precipitation and MCSs in the Peruvian Central Andes, a region with complex terrain, two CPM regional climate simulations are run using the WRF model and two PBL schemes, namely ACM2 and MYNN, over a 6-year period (2014–2019) with the first year treated as a spin-up period. These simulations are at a grid spacing of 15 km covering the entire South America and a nested convection-permitting grid spacing of 3 km covering the Peruvian central Andes region. The ERA5 reanalysis data are used to provide the lateral boundary conditions for the 15-km grid. These two CPM simulations combined with the SAAG 4-km simulation covering the entire South America and using the YSU PBL scheme, rain gauge data in Peru and Brazil, and three gridded global precipitation datasets, are used to study the characteristics of precipitation and MCSs in the Peruvian central Andes region and evaluate the capability of models in replicating key observed characteristics. This study provides the evidence on the feasibility of CPM simulations thus configured for projecting the potential impacts of climate change on precipitation and MCSs in this region while pointing out certain deficiencies. The major results are summarized as follows.

(1) All three simulations, the two 3-km simulations (WRF3km_ACM2 and WRF3km_MYNN) and the 4-km simulation (WRF4km_SAAG), broadly capture the seasonal spatiotemporal patterns of precipitation, particularly the hotspots associated with the prevailing winds and terrain features along the east slope of the Peruvian Central Andes, although some biases in specific precipitation values are present. Among the simulations, WRF3km_MYNN generally outperforms the other two simulations over the mountain regions compared to the gridded precipitation products and available rain gauge data. Meanwhile, WRF3km_MYNN and WRF4km_SAAG display comparable performance in the western Amazon Basin region.

(2) The three simulations also effectively replicate the sub-daily spatiotemporal patterns of precipitation, but biases in precipitation intensity are evident. When taking into account both the spatial distribution and intensity of diurnal precipitation, WRF3km_MYNN generally outperforms the other two simulations in the mountain region. Both WRF3km_MYNN and particularly WRF4km_SAAG demonstrate superior performance in the western Amazon region when compared to gridded precipitation products and available rain gauge data in Brazil.

(3) The simulations generally replicate the observed spatiotemporal patterns and propagation of MCSs, particularly along the east slope of the Peruvian Central Andes and over the western Amazon Basin, across both seasonal and diurnal time scales. However, specific discrepancies exist in MCS genesis frequency and movement speed. For instance, WRF3km_ACM2 notably underestimates the frequency of MCSs, particularly during the warm seasons of 2016 and 2019. Conversely, WRF3km_MYNN and WRF4km_SAAG tend to overestimate MCS frequency during the warm season. Additionally, all three simulations consistently depict higher frequencies of MCSs with higher moving speeds than those observed in IMERG and CMORPH, highlighting areas for model improvement. Nonetheless, uncertainties do exist with the IMERG and CMORPH precipitation estimate products, and more robust precipitation observations are needed to obtain more reliable evaluations.

(4) Statistical analyses of MCS properties reveal that the simulations generally overestimate both mean and peak hourly precipitation intensity associated with the MCSs, and produce smaller MCS sizes but similar total hourly precipitation volumes compared to the gridded precipitation products. Moreover, all datasets agree on a median MCS duration of ~ 3 hours within the study area, and the simulations generally produce faster MCS moving speeds compared to the gridded precipitation products.

(5) Analyses of the diurnal variations in dynamic and thermodynamic parameters indicate that dynamic factors, mainly LLJ-terrain-induced uplift of moisture and energy, are the principal drivers for MCS genesis along the east slopes of the Andes. While in the western Amazon Basin, MCSs predominantly form in the afternoon and are largely governed by

thermodynamic factors, specifically solar radiation-induced diurnal changes in CAPE and CIN. The lower CAPE and higher CIN along with weaker convergence in WRF3km_ACM2 result in weaker precipitation and fewer MCSs than in WRF3km_MYNN. These differences are attributed to the differences in vertical mixing within the PBL and especially entrainment flux at the PBL top in different PBL schemes. They impact the vertical transportation of moisture and momentum, then cloud formation and cloud fraction, and ultimately surface radiative heating, CAPE, and precipitation, analyzed previously based on shorter-term simulations (Huang et al., 2023; X.-M. Hu et al., 2023). Besides, similar thermodynamic effects are observed to be the dominant influence on precipitation over elevated mountains.

In summary, the investigation of precipitation and MCS characteristics in the Peruvian Central Andes in this study offers valuable insights into both observed patterns and convection-permitting regional climate simulation performances. The findings not only enhance our understanding of the specific precipitation and MCS characteristics within this region, but also document the differences between observations and the WRF simulations, which can inform future model improvements. It should be noted that the discrepancies between the gridded precipitation products and the simulations may also arise from the uncertainties and low effective resolutions of the gridded precipitation products (Guilloteau & Foufoula-Georgiou, 2020), thereby emphasizing the need for more reliable observational products. Despite the presence of biases, the CPM simulations effectively capture the fundamental mechanisms that govern precipitation and convective systems in the Peruvian Central Andes region. It suggests the feasibility of CPM simulations for projecting the potential impacts of climate change on precipitation and MCSs in the region, thereby providing critical input for tailored climate adaptation strategies in this region, especially after bias correction/calibration of the model projections. Two future climate simulations have been conducted using the same model configuration as WRF3km_MYNN, focusing on two shared socioeconomic pathway (SSP) scenarios, SSP2-4.5 and SSP5-8.5, that represent the medium and high emission scenarios, respectively. The choice of the WRF3km_MYNN configuration was based on the evaluations of the historical simulations reported in Huang et al. (2023), X.-M. Hu et al. (2023), and this study. These simulations are driven by a bias-corrected global dataset, derived from a CMIP6 multi-model ensemble (Xu et al., 2021). The SAAG future simulation is running as well using a pseudo global warming approach and targeting a warming level of $\sim 2.5^{\circ}\text{C}$ in the period of 2060–2080 over South America (Dominguez et al., 2023). Projected changes in precipitation and MCSs in the Peruvian Central Andes region, based on these CPM simulations, will be analyzed and reported in the future.

Open Research Section

ERA5 reanalysis data are available at <https://doi.org/10.5065/BH6N-5N20>. GPM IMERG Final Precipitation dataset is available at <https://doi.org/10.5067/GPM/IMERGDF/DAY/06> (last access: 12 November 2020). CMORPH dataset is available at https://ftp.cpc.ncep.noaa.gov/precip/CMORPH_V1.0/CRT/8km-30min (last access: 12 November 2020). MSWEP dataset is available at <http://www.gloh2o.org/mswep> (last access: 17 July 2021). The rain gauge data in Peru are available at <https://piscoprec.github.io/webPISCO/en/raingauges> (last access: 18 July 2021). The rain gauge data in Brazil are available at <https://bdmep.inmet.gov.br> (last access: 19 January 2023). The SAAG 4-km simulation dataset is available at <https://ral.ucar.edu/projects/south-america-affinity-group-saag/model-output> (last access: 18 July 2022). The model outputs are too large to be publicly archived. Please contact the corresponding author for more information.

Acknowledgments

This project was primarily supported by grant No. 20163646499 from the Universidad Nacional de San Agustín de Arequipa (UNSA) of Peru through the IREES/LASI Global Change and Human Health Institute. Supplementary funding was provided by the Weath-

ernews Chair funds. Yongjie Huang is partially supported by the DOE ASR project (DE-SC0024317). The authors acknowledge the Texas Advanced Computing Center (TACC) at the University of Texas at Austin (<http://www.tacc.utexas.edu>) for providing HPC resources through XSEDE allocation TG-ATM160014 that are used for the simulations. The authors also acknowledge high-performance computing support from Cheyenne (<https://doi.org/10.5065/D6RX99HX>) provided by NCAR’s Computational and Information Systems Laboratory. NCAR is sponsored by the National Science Foundation. Some data processing was performed at the University of Oklahoma (OU) Supercomputing Center for Education and Research (OSCAR).

References

- Anselmo, E. M., Machado, L. A., Schumacher, C., & Kiladis, G. N. (2021). Amazonian mesoscale convective systems: Life cycle and propagation characteristics. *International Journal of Climatology*, 41(7), 3968–3981. doi: 10.1002/joc.7053
- Arias, P. A., Garreaud, R., Poveda, G., Espinoza, J. C., Molina-Carpio, J., Masiokas, M., ... Van Oevelen, P. J. (2021). Hydroclimate of the andes part ii: Hydroclimate variability and sub-continental patterns. *Frontiers in Earth Science*, 8, 666. doi: 10.3389/feart.2020.505467
- Aybar, C., Fernández, C., Huerta, A., Lavado, W., Vega, F., & Felipe-Obando, O. (2020). Construction of a high-resolution gridded rainfall dataset for peru from 1981 to the present day. *Hydrological Sciences Journal*, 65(5), 770–785. doi: 10.1080/02626667.2019.1649411
- Barlage, M., Chen, F., Rasmussen, R., Zhang, Z., & Miguez-Macho, G. (2021). The importance of scale-dependent groundwater processes in land-atmosphere interactions over the central united states. *Geophysical Research Letters*, 48(5), e2020GL092171. doi: 10.1029/2020GL092171
- Beck, H. E., Wood, E. F., Pan, M., Fisher, C. K., Miralles, D. G., Van Dijk, A. I., ... Adler, R. F. (2019). Mswep v2 global 3-hourly 0.1 precipitation: methodology and quantitative assessment. *Bulletin of the American Meteorological Society*, 100(3), 473–500. doi: 10.1175/BAMS-D-17-0138.1
- Berthou, S., Kendon, E. J., Chan, S. C., Ban, N., Leutwyler, D., Schär, C., & Fosser, G. (2020). Pan-european climate at convection-permitting scale: a model intercomparison study. *Climate Dynamics*, 55(1), 35–59. doi: 10.1007/s00382-018-4114-6
- Bettoli, M. L., Solman, S. A., Da Rocha, R., Llopart, M., Gutierrez, J. M., Fernández, J., ... others (2021). The cordex flagship pilot study in southeastern south america: a comparative study of statistical and dynamical downscaling models in simulating daily extreme precipitation events. *Climate Dynamics*, 56, 1589–1608. doi: 10.1007/s00382-020-05549-z
- Blackadar, A. K. (1957). Boundary layer wind maxima and their significance for the growth of nocturnal inversions. *Bulletin of the American Meteorological Society*, 38(5), 283–290. doi: 10.1175/1520-0477-38.5.283
- Carbone, R., & Tuttle, J. (2008). Rainfall occurrence in the us warm season: The diurnal cycle. *Journal of Climate*, 21(16), 4132–4146. doi: 10.1175/2008JCLI2275.1
- Chavez, S. P., Silva, Y., & Barros, A. P. (2020). High-elevation monsoon precipitation processes in the central andes of peru. *Journal of Geophysical Research: Atmospheres*, 125(24), e2020JD032947. doi: 10.1029/2020JD032947
- Chen, M., Huang, Y., Li, Z., Larico, A. J. M., Xue, M., Hong, Y., ... others (2022). Cross-examining precipitation products by rain gauge, remote sensing, and wrf simulations over a south american region across the pacific coast and andes. *Atmosphere*, 13(10), 1666. doi: 10.3390/atmos13101666
- Condom, T., Martínez, R., Pabón, J. D., Costa, F., Pineda, L., Nieto, J. J., ... Villacis, M. (2020). Climatological and hydrological observations for the south american andes: in situ stations, satellite, and reanalysis data sets. *Frontiers in Earth Science*, 8, 92. doi: 10.3389/feart.2020.00092

- Corfidi, S. F. (2003). Cold pools and mcs propagation: Forecasting the motion of downwind-developing mcscs. *Weather and forecasting*, 18(6), 997–1017. doi: 10.1175/1520-0434(2003)018<0997:CPAMPF>2.0.CO;2
- Dominguez, F., Rasmussen, R., Liu, C., Ikeda, K., Prein, A., Varble, A., ... others (2023). Advancing south american water and climate science through multi-decadal convection-permitting modeling. *Bulletin of the American Meteorological Society*. doi: 10.1175/BAMS-D-22-0226.1
- Drenkhan, F., Carey, M., Huggel, C., Seidel, J., & Oré, M. T. (2015). The changing water cycle: climatic and socioeconomic drivers of water-related changes in the andes of peru. *Wiley Interdisciplinary Reviews: Water*, 2(6), 715–733. doi: 10.1002/wat2.1105
- Ek, M., Mitchell, K., Lin, Y., Rogers, E., Grunmann, P., Koren, V., ... Tarpley, J. (2003). Implementation of noah land surface model advances in the national centers for environmental prediction operational mesoscale eta model. *Journal of Geophysical Research: Atmospheres*, 108(D22). doi: 10.1029/2002JD003296
- Espinoza, J. C., Chavez, S., Ronchail, J., Junquas, C., Takahashi, K., & Lavado, W. (2015). Rainfall hotspots over the southern tropical andes: Spatial distribution, rainfall intensity, and relations with large-scale atmospheric circulation. *Water Resources Research*, 51(5), 3459–3475. doi: 10.1002/2014WR016273
- Feng, Z., Leung, L. R., Liu, N., Wang, J., Houze Jr, R. A., Li, J., ... Guo, J. (2021). A global high-resolution mesoscale convective system database using satellite-derived cloud tops, surface precipitation, and tracking. *Journal of Geophysical Research: Atmospheres*, 126(8), e2020JD034202. doi: 10.1029/2020JD034202
- Fosser, G., Khodayar, S., & Berg, P. (2015). Benefit of convection permitting climate model simulations in the representation of convective precipitation. *Climate Dynamics*, 44(1–2), 45–60. doi: 10.1007/s00382-014-2242-1
- Fumière, Q., Déqué, M., Nuissier, O., Somot, S., Alias, A., Caillaud, C., ... Seity, Y. (2020). Extreme rainfall in mediterranean france during the fall: added value of the cnrm-arome convection-permitting regional climate model. *Climate Dynamics*, 55(1), 77–91. doi: 10.1007/s00382-019-04898-8
- Gao, Y., Leung, L. R., Zhao, C., & Hagos, S. (2017). Sensitivity of us summer precipitation to model resolution and convective parameterizations across gray zone resolutions. *Journal of Geophysical Research: Atmospheres*, 122(5), 2714–2733. doi: 10.1002/2016JD025896
- Giorgi, F. (2019). Thirty years of regional climate modeling: where are we and where are we going next? *Journal of Geophysical Research: Atmospheres*, 124(11), 5696–5723. doi: 10.1029/2018JD030094
- Gonzalez, F. R., Raval, S., Taplin, R., Timms, W., & Hitch, M. (2019). Evaluation of impact of potential extreme rainfall events on mining in peru. *Natural Resources Research*, 28, 393–408. doi: 10.1007/s11053-018-9396-1
- Guilloteau, C., & Foufoula-Georgiou, E. (2020). Multiscale evaluation of satellite precipitation products: Effective resolution of imerg. *Satellite Precipitation Measurement: Volume 2*, 533–558. doi: 10.1007/978-3-030-35798-6_5
- Guo, Z., Fang, J., Sun, X., Tang, J., Yang, Y., & Tang, J. (2020). Decadal long convection-permitting regional climate simulations over eastern china: evaluation of diurnal cycle of precipitation. *Climate Dynamics*, 54(3), 1329–1349. doi: 10.1007/s00382-019-05061-z
- Halladay, K., Kahana, R., Johnson, B., Still, C., Fosser, G., & Alves, L. (2023). Convection-permitting climate simulations for south america with the met office unified model. *Climate Dynamics*, 1–23. doi: 10.1007/s00382-023-06853-0
- Heikenfeld, M., Marinescu, P. J., Christensen, M., Watson-Parris, D., Senf, F., van den Heever, S. C., & Stier, P. (2019). tobac 1.2: towards a flexible framework for tracking and analysis of clouds in diverse datasets. *Geoscientific Model Development*, 12(11), 4551–4570. doi: 10.5194/gmd-12-4551-2019
- Hersbach, H., Bell, B., Berrisford, P., Hirahara, S., Horányi, A., Muñoz-Sabater, J., ... others (2020). The era5 global reanalysis. *Quarterly Journal of the Royal Meteorological*

- Society*, 146(730), 1999–2049. doi: 10.1002/qj.3803
- Hong, S.-Y., & Lim, J.-O. J. (2006). The wrf single-moment 6-class microphysics scheme (wsm6). *Asia-Pacific Journal of Atmospheric Sciences*, 42(2), 129–151.
- Houze Jr, R. A. (2004). Mesoscale convective systems. *Reviews of Geophysics*, 42(4). doi: 10.1029/2004RG000150
- Houze Jr, R. A. (2018). 100 years of research on mesoscale convective systems. *Meteorological Monographs*, 59, 17–1. doi: 10.1175/AMSMONOGRAPH-D-18-0001.1
- Hu, H., Leung, L. R., & Feng, Z. (2021). Early warm-season mesoscale convective systems dominate soil moisture–precipitation feedback for summer rainfall in central united states. *Proceedings of the National Academy of Sciences*, 118(43), e2105260118. doi: 10.1073/pnas.2105260118
- Hu, X.-M., Huang, Y., Xue, M., Martin, E., Hong, Y., Chen, M., ... others (2023). Effects of lower troposphere vertical mixing on simulated clouds and precipitation over the amazon during the wet season. *Journal of Geophysical Research: Atmospheres*, 128(12), e2023JD038553. doi: 10.1029/2023JD038553
- Huang, Y., Xue, M., Hu, X.-M., Martin, E., Novoa, H. M., McPherson, R. A., ... Morales, I. Y. (2023). Convection-permitting simulations of precipitation over the peruvian central andes: Strong sensitivity to planetary boundary layer parameterization. *Journal of Hydrometeorology*, 24(11), 1969–1990. doi: 10.1175/JHM-D-22-0173.1
- Huffman, G., Stocker, E., Bolvin, D., Nelkin, E., & Tan, J. (2019). Gpm imerg final precipitation 13 1 day 0.1 degree x 0.1 degree v06, edited by andrey savtchenko, greenbelt, md, goddard earth sciences data and information services center (ges disc). , Accessed: [12 November 2020]. doi: 10.5067/GPM/IMERGDF/DAY/06
- Hwang, Y., Zhao, X., You, C.-H., & Li, Y. (2023). Climatological features of future mcsc in convection-permitting climate models using cmip6 and era5 in the central united states. *Quarterly Journal of the Royal Meteorological Society*. doi: 10.1002/qj.4549
- Iacono, M. J., Delamere, J. S., Mlawer, E. J., Shephard, M. W., Clough, S. A., & Collins, W. D. (2008). Radiative forcing by long-lived greenhouse gases: Calculations with the aer radiative transfer models. *Journal of Geophysical Research: Atmospheres*, 113(D13). doi: 10.1029/2008JD009944
- Jiménez, P. A., Dudhia, J., González-Rouco, J. F., Navarro, J., Montávez, J. P., & García-Bustamante, E. (2012). A revised scheme for the wrf surface layer formulation. *Monthly Weather Review*, 140(3), 898–918. doi: 10.1175/MWR-D-11-00056.1
- Jones, C. (2019). Recent changes in the south america low-level jet. *Npj Climate and Atmospheric Science*, 2(1), 20. doi: 10.1038/s41612-019-0077-5
- Joyce, R. J., Janowiak, J. E., Arkin, P. A., & Xie, P. (2004). Cmorph: A method that produces global precipitation estimates from passive microwave and infrared data at high spatial and temporal resolution. *Journal of hydrometeorology*, 5(3), 487–503. doi: 10.1175/1525-7541(2004)005<0487:CAMTPG>2.0.CO;2
- Jukes, M., Taylor, K. E., Durack, P. J., Lawrence, B., Mizielinski, M. S., Pamment, A., ... Sényi, S. (2020). The cmip6 data request (dreq, version 01.00. 31). *Geoscientific Model Development*, 13(1), 201–224. doi: 10.5194/gmd-13-201-2020
- Junquas, C., Heredia, M., Condom, T., Ruiz-Hernández, J., Campozano, L., Dudhia, J., ... Sicart, J.-E. (2022). Regional climate modeling of the diurnal cycle of precipitation and associated atmospheric circulation patterns over an andean glacier region (antisana, ecuador). *Climate Dynamics*, 58(11-12), 3075–3104. doi: 10.1007/s00382-021-06079-y
- Junquas, C., Takahashi, K., Condom, T., Espinoza, J.-C., Chávez, S., Sicart, J.-E., & Lebel, T. (2018). Understanding the influence of orography on the precipitation diurnal cycle and the associated atmospheric processes in the central andes. *Climate dynamics*, 50, 3995–4017. doi: 10.1007/s00382-017-3858-8
- Karki, R., Gerlitz, L., Schickhoff, U., Scholten, T., Böhner, J., et al. (2017). Quantifying the added value of convection-permitting climate simulations in complex terrain: a systematic evaluation of wrf over the himalayas. *Earth System Dynamics*, 8(3), 507–528. doi: 10.5194/esd-8-507-2017

- Kendon, E., Prein, A., Senior, C., & Stirling, A. (2021). Challenges and outlook for convection-permitting climate modelling. *Philosophical Transactions of the Royal Society A*, 379(2195), 20190547. doi: 10.1098/rsta.2019.0547
- Kouadio, K., Bastin, S., Konare, A., & Ajayi, V. O. (2020). Does convection-permitting simulate better rainfall distribution and extreme over guinean coast and surroundings? *Climate Dynamics*, 55(1), 153–174. doi: 10.1007/s00382-018-4308-y
- Kukulies, J., Chen, D., & Curio, J. (2021). The role of mesoscale convective systems in precipitation in the tibetan plateau region. *Journal of Geophysical Research: Atmospheres*, 126(23), e2021JD035279. doi: 10.1029/2021JD035279
- Lavin-Gullon, A., Feijoó, M., Solman, S., Fernández, J., da Rocha, R., & Bettolli, M. L. (2021). Synoptic forcing associated with extreme precipitation events over south-eastern south america as depicted by a cortex fps set of convection-permitting rms. *Climate Dynamics*, 56, 3187–3203. doi: 10.1007/s00382-021-05637-8
- Li, P., Furtado, K., Zhou, T., Chen, H., & Li, J. (2021). Convection-permitting modelling improves simulated precipitation over the central and eastern tibetan plateau. *Quarterly Journal of the Royal Meteorological Society*, 147(734), 341–362. doi: 10.1002/qj.3921
- Li, P., Moseley, C., Prein, A. F., Chen, H., Li, J., Furtado, K., & Zhou, T. (2020). Mesoscale convective system precipitation characteristics over east asia. part i: Regional differences and seasonal variations. *Journal of Climate*, 33(21), 9271–9286. doi: 10.1175/JCLI-D-20-0072.1
- Lind, P., Belušić, D., Christensen, O. B., Dobler, A., Kjellström, E., Landgren, O., ... others (2020). Benefits and added value of convection-permitting climate modeling over fenno-scandinavia. *Climate Dynamics*, 55(7), 1893–1912. doi: 10.1007/s00382-020-05359-3
- Liu, C., Ikeda, K., Rasmussen, R., Barlage, M., Newman, A. J., Prein, A. F., ... others (2017). Continental-scale convection-permitting modeling of the current and future climate of north america. *Climate Dynamics*, 49(1), 71–95. doi: 10.1007/s00382-016-3327-9
- Marengo, J. A., Douglas, M. W., & Silva Dias, P. L. (2002). The south american low-level jet east of the andes during the 1999 lba-trmm and lba-wet amc campaign. *Journal of Geophysical Research: Atmospheres*, 107(D20), LBA–47. doi: 10.1029/2001JD001188
- Martínez, A., Takahashi, K., Núñez, E., Silva, Y., Trasmonte, G., Mosquera, K., & Lagos, P. (2008). A multi-institutional and interdisciplinary approach to the assessment of vulnerability and adaptation to climate change in the peruvian central andes: problems and prospects. *Advances in Geosciences*, 14, 257–260. doi: 10.5194/adgeo-14-257-2008
- Miguez-Macho, G., Fan, Y., Weaver, C. P., Walko, R., & Robock, A. (2007). Climate and dynamics: D13108-incorporating water table dynamics in climate modeling: 2. formulation, validation, and soil moisture simulation (doi 10.1029/2006jd008112). *Journal of Geophysical Research-Part D-Atmospheres*, 112(13). doi: 10.1029/2006JD008112
- Mohr, K. I., Slayback, D., & Yager, K. (2014). Characteristics of precipitation features and annual rainfall during the trmm era in the central andes. *Journal of climate*, 27(11), 3982–4001. doi: 10.1175/JCLI-D-13-00592.1
- Nakanishi, M., & Niino, H. (2009). Development of an improved turbulence closure model for the atmospheric boundary layer. *Journal of the Meteorological Society of Japan. Ser. II*, 87(5), 895–912. doi: 10.2151/jmsj.87.895
- Niu, G.-Y., Yang, Z.-L., Mitchell, K. E., Chen, F., Ek, M. B., Barlage, M., ... others (2011). The community noah land surface model with multiparameterization options (noah-mp): 1. model description and evaluation with local-scale measurements. *Journal of Geophysical Research: Atmospheres*, 116(D12). doi: 10.1029/2010JD015139
- Paccini, L., & Stevens, B. (2023). Assessing precipitation over the amazon basin as simulated by a storm-resolving model. *Journal of Geophysical Research: Atmospheres*, 128(4), e2022JD037436. doi: 10.1029/2022JD037436

- Pleim, J. E. (2007). A combined local and nonlocal closure model for the atmospheric boundary layer. part i: Model description and testing. *Journal of Applied Meteorology and Climatology*, 46(9), 1383–1395. doi: 10.1175/JAM2539.1
- Poveda, G., Espinoza, J. C., Zuluaga, M. D., Solman, S. A., Garreaud, R., & Van Oevelen, P. J. (2020). High impact weather events in the andes. *Frontiers in Earth Science*, 8, 162. doi: 10.3389/feart.2020.00162
- Prein, A., Gobiet, A., Suklitsch, M., Truhetz, H., Awan, N., Keuler, K., & Georgievski, G. (2013). Added value of convection permitting seasonal simulations. *Climate Dynamics*, 41(9-10), 2655–2677. doi: 10.1007/s00382-013-1744-6
- Prein, A. F., Liu, C., Ikeda, K., Bullock, R., Rasmussen, R. M., Holland, G. J., & Clark, M. (2020). Simulating north american mesoscale convective systems with a convection-permitting climate model. *Climate Dynamics*, 55, 95–110. doi: 10.1007/s00382-017-3993-2
- Prein, A. F., Liu, C., Ikeda, K., Trier, S. B., Rasmussen, R. M., Holland, G. J., & Clark, M. P. (2017). Increased rainfall volume from future convective storms in the us. *Nature Climate Change*, 7(12), 880–884. doi: 10.1038/s41558-017-0007-7
- Roca, R., & Fiolleau, T. (2020). Extreme precipitation in the tropics is closely associated with long-lived convective systems. *Communications Earth & Environment*, 1(1), 18. doi: 10.1038/s43247-020-00015-4
- Romatschke, U., & Houze Jr, R. A. (2010). Extreme summer convection in south america. *Journal of Climate*, 23(14), 3761–3791. doi: 10.1175/2010JCLI3465.1
- Salio, P., Nicolini, M., & Zipser, E. J. (2007). Mesoscale convective systems over southeastern south america and their relationship with the south american low-level jet. *Monthly Weather Review*, 135(4), 1290–1309. doi: 10.1175/MWR3305.1
- Schumacher, R. S., & Rasmussen, K. L. (2020). The formation, character and changing nature of mesoscale convective systems. *Nature Reviews Earth & Environment*, 1(6), 300–314. doi: 10.1038/s43017-020-0057-7
- Schumacher, V., Fernández, A., Justino, F., & Comin, A. (2020). Wrf high resolution dynamical downscaling of precipitation for the central andes of chile and argentina. *Frontiers in Earth Science*, 8, 328. doi: 10.3389/feart.2020.00328
- Schwartz, C. S., Romine, G. S., Fossell, K. R., Sobash, R. A., & Weisman, M. L. (2017). Toward 1-km ensemble forecasts over large domains. *Monthly Weather Review*, 145(8), 2943–2969. doi: 10.1175/MWR-D-16-0410.1
- Skamarock, W. C., Klemp, J. B., Dudhia, J., Gill, D. O., Liu, Z., Berner, J., ... others (2019). A description of the advanced research wrf model version 4. *National Center for Atmospheric Research: Boulder, CO, USA*, 145. doi: 10.5065/1dfh-6p97
- Stratton, R. A., Senior, C. A., Vosper, S. B., Folwell, S. S., Boutle, I. A., Earnshaw, P. D., ... others (2018). A pan-african convection-permitting regional climate simulation with the met office unified model: Cp4-africa. *Journal of Climate*, 31(9), 3485–3508. doi: 10.1175/JCLI-D-17-0503.1
- Sun, X., Xue, M., Brotzge, J., McPherson, R. A., Hu, X.-M., & Yang, X.-Q. (2016). An evaluation of dynamical downscaling of central plains summer precipitation using a wrf-based regional climate model at a convection-permitting 4 km resolution. *Journal of Geophysical Research: Atmospheres*, 121(23), 13–801. doi: 10.1002/2016JD024796
- Thompson, G., Field, P. R., Rasmussen, R. M., & Hall, W. D. (2008). Explicit forecasts of winter precipitation using an improved bulk microphysics scheme. part ii: Implementation of a new snow parameterization. *Monthly Weather Review*, 136(12), 5095–5115. doi: 10.1175/2008MWR2387.1
- Tiedtke, M. (1989). A comprehensive mass flux scheme for cumulus parameterization in large-scale models. *Monthly weather review*, 117(8), 1779–1800. doi: 10.1175/1520-0493(1989)117<1779:ACMFSF>2.0.CO;2
- Vera, C., Baez, J., Douglas, M., Emmanuel, C., Marengo, J., Meitin, J., ... others (2006). The south american low-level jet experiment. *Bulletin of the American Meteorological Society*, 87(1), 63–78. doi: 10.1175/BAMS-87-1-63
- Vergara, W., Deeb, A., Leino, I., Kitoh, A., & Escobar, M. (2011). *Assessment of the impacts*

- of climate change on mountain hydrology: development of a methodology through a case study in the andes of peru. World Bank Publications. doi: 10.1596/978-0-8213-8662-0
- Vernekar, A. D., Kirtman, B. P., & Fennessy, M. J. (2003). Low-level jets and their effects on the south american summer climate as simulated by the ncep eta model. *Journal of Climate*, 16(2), 297–311. doi: 10.1175/1520-0442(2003)016<0297:LLJATE>2.0.CO;2
- Xu, Z., Han, Y., Tam, C.-Y., Yang, Z.-L., & Fu, C. (2021). Bias-corrected cmip6 global dataset for dynamical downscaling of the historical and future climate (1979–2100). *Scientific Data*, 8(1), 293. doi: 10.1038/s41597-021-01079-3
- Xue, M., Luo, X., Zhu, K., Sun, Z., & Fei, J. (2018). The controlling role of boundary layer inertial oscillations in meiyu frontal precipitation and its diurnal cycles over china. *Journal of Geophysical Research: Atmospheres*, 123(10), 5090–5115. doi: 10.1029/2018JD028368
- Zhao, M. (2022). A study of ar-, ts-, and mcs-associated precipitation and extreme precipitation in present and warmer climates. *Journal of Climate*, 35(2), 479–497. doi: 10.1175/JCLI-D-21-0145.1
- Zhao, Y., Xue, M., Jiang, J., Hu, X.-M., & Huang, A. (2023). Assessment of wet season precipitation in the central united states by the regional climate simulation of the wrfg member in narccap and its relationship with large-scale circulation biases. *ADVANCES IN ATMOSPHERIC SCIENCES*, 41. doi: 10.1007/s00376-023-2353-x
- Zhu, K., Xue, M., Zhou, B., Zhao, K., Sun, Z., Fu, P., ... Meng, Q. (2018). Evaluation of real-time convection-permitting precipitation forecasts in china during the 2013–2014 summer season. *Journal of Geophysical Research: Atmospheres*, 123(2), 1037–1064. doi: 10.1002/2017JD027445